Generated using the official AMS LaTeX template v6.1

Estimation of Surface Current Divergence from Satellite Doppler Radar Scatterometer Measurements of Surface Ocean Velocity

Dudley B. Chelton

College of Earth, Ocean and Atmospheric Sciences, Oregon State University, Corvallis, Oregon

April 25, 2023

Corresponding author: Dudley B. Chelton, dudley.chelton@oregonstate.edu

ABSTRACT: The ability to estimate the divergence and vorticity of surface ocean velocity from space is assessed from simulated satellite Doppler scatterometer measurements of surface currents with a footprint diameter of 5 km across an 1800-km measurement swath. The focus is on non-internal-wave contributions to surface divergence and vorticity. This is achieved by simulating Doppler scatterometer measurements of surface currents from a numerical model in which internal waves are weak because of high dissipation, seasonal cycle forcing and the lack of tidal forcing. Divergence is much more challenging to estimate than vorticity because the signals are weaker and restricted to smaller scales. For the measurement noise that was anticipated based on early engineering studies, a previous analysis by Chelton et al. (2019) was pessimistic about the ability to estimate surface current divergence with useful spatial and temporal resolutions. That study therefore considered only the estimation of surface current vorticity. Recent technological developments and an improved understanding of how the errors in measurements of surface currents depend on the ambient wind speed have concluded that the measurement noise can be substantially reduced in conditions of wind speed greater than about 6 m s^{-1}. For reference, the globally averaged wind speed over the ocean is 7.4 m s^{-1}. A reassessment of the ability to estimate non-internal-wave contributions to surface current divergence from Doppler scatterometer data in this study finds that useful estimates can be obtained in sufficiently high winds. Moreover, the improved measurement accuracy will also provide significantly higher-resolution estimates of surface current vorticity than was previously thought.

1. Introduction

The advent of Doppler radar scatterometry promises to revolutionize studies of air-sea interaction by providing the first satellite observations of surface ocean velocity. These surface current measurements will be collocated with measurements of surface vector winds over the global ocean. Wind speed and direction will be obtained by conventional scatterometry from the power of the radar backscatter measurements from multiple antenna viewing angles (see, for example, Section 2 of Chelton and Freilich 2005), but at a Ka-band frequency of 38.5 GHz, compared with the Ku-band frequency of 13.4 GHz for the QuikSCAT scatterometer. The higher frequency in combination with a larger antenna size (Rodríguez et al. 2019) allows a smaller footprint diameter of 5 km, compared with 25 km for QuikSCAT. Analogous to coastal radar systems, surface current velocity will be estimated by measuring the Doppler shift of the frequency of the radar returns along multiple antenna viewing angles (Chapron et al. 2005; Ardhuin et al. 2018; Rodríguez 2018). The viability of the technology has been demonstrated from the airborne DopplerScatt instrument (Rodríguez et al. 2018) that was designed and built at the NASA Jet Propulsion Laboratory and has been used in the field campaigns of the Sub-Mesoscale Ocean Dynamics Experiment (S-MODE) (Farrar et al. 2020).

The future satellite Doppler scatterometer mission that is considered in this study is in the early stages of development by NASA and has been given the tentative name ODYSEA (Ocean DYnamics and Surface Exchange with the Atmosphere). Following Rodríguez (2018), Chelton et al. (2019), Rodríguez et al. (2019), Villas Bôas et al. (2019) and Wineteer et al. (2020), it will be referred to here generically by the acronym WaCM (Winds and Currents Mission) that succinctly describes what the instrument will measure. While the primary goal of WaCM is to measure surface currents and winds, an exciting additional prospect from such a mission is the ability to estimate the relative vorticity $\zeta = \partial v/\partial x - \partial u/\partial y$ (referred to hereinafter as vorticity) and divergence $\delta = \partial u/\partial x + \partial v/\partial y$ of surface currents from horizontal derivatives of the x and y surface velocity components u and v. The capabilities for estimation of surface current vorticity have been investigated by Chelton et al. (2019), referred to hereinafter as C19. The goal of this study is to extend that analysis to investigate the capabilities for estimation of the surface current divergence that is directly related to near-surface vertical velocity and thus has important implications for air-sea exchange of CO_2 and other gasses, as well as the supply of nutrients from depth that are critical to biological productivity.

Estimation of derivative quantities poses a challenge because of the amplification of measurement noise by centered difference approximations of the derivatives (see, for example, appendix G.2 of C19 for a detailed propagation-of-error analysis of the noise in vorticity estimated from noisy WaCM measurements of surface current velocity). Spatial and/or temporal smoothing will be required to reduce the noise sufficiently for the estimates of divergence and vorticity to be scientifically useful. The degree of smoothing that will be needed depends on the relative magnitudes of the signal variability and the measurement errors. For example, a measurement noise standard deviation of 0.25 m s^{-1} that was considered by C19 requires spatial smoothing of the noisy velocity fields with a half-power filter cutoff wavelength of at least 50 km to obtain useful instantaneous snapshot maps of vorticity in the California Current region (see Fig. 44 of that study). A higher noise standard deviation of 0.50 m s^{-1} requires a spatial smoothing of more than 100 km. The spatial resolution can be improved somewhat by averaging temporally (see Fig. 45 of that study), but at the costs of reduced temporal resolution and the addition of sampling errors from unresolved high-frequency variability.

Estimation of surface current divergence is much more difficult than estimation of vorticity. Because the ocean is quasi-geostrophic on scales larger than the Rossby radius of deformation, which is 25–30 km in the California Current region considered in this study (see Fig. 6 of Chelton et al. 1998), the currents are nearly non-divergent. It can therefore be anticipated that the resolution capability of surface current divergence estimated from noisy WaCM measurements of surface velocity will be coarser than that of surface current vorticity. As the most energetic divergence signals occur at short submesoscales (see Fig. 2 in section 2 below), the spatial smoothing required to reduce the noise also attenuates much of the divergence signals that are of interest. For a standard deviation of 0.25 m s^{-1} for surface velocity measurements, application of the method suggested by C19 (and used in this study) to assess resolution capability concluded that WaCM measurements would have to be smoothed by more than 200 km to obtain scientifically useful estimates of divergence, even in 16-day averages. In most regions of the world ocean, there is very little surface current divergence signal on scales this large. Divergence was therefore not considered by C19.

A recent analysis of simulated WaCM measurements of surface currents by Wineteer et al. (2020) came to the surprising conclusion that the resolution capability of divergence in the California Current region is about 50 km. In part, this is because of improvements in the expected accuracy of the surface current measurements as a result of continued technological developments, refinements of the retrieval algorithms, and advances in the understanding of how the noise in surface current measurements depends on wind speed. In conditions of wind speeds higher than about 6 m s^{-1}, which can be compared with the global average wind speed of 7.4 m s^{-1} (Wentz et al. 1986), it may be possible to achieve a measurement noise standard deviation of 0.10 m s^{-1}, at least in the middle portion of each of the two measurement swaths that straddle the satellite ground track (see Fig. 2 of Wineteer et al. 2020). Wineteer et al. (2020) speculate that the surprisingly high resolution capability for estimates of divergence is likely also attributable to the fact that the numerical model used to simulate WaCM data in their analysis includes highly energetic internal waves that contribute more than other submesoscale process to surface divergence field. In contrast, the model used by C19 to simulate WaCM data was forced by seasonal cycle winds and does not include tidal forcing. Internal waves, as well as inertial motions, are therefore weak in that model.

The improved accuracy of WaCM measurements of surface currents reported by Wineteer et al. (2020) has motivated a reassessment of how well surface current divergence, as well as vorticity, can be estimated from a future satellite Doppler scatterometer mission. While much remains to be learned about internal waves, most applications of WaCM data will likely focus more on the surface currents, divergence and vorticity that are associated with other submesoscale and mesoscale processes. To investigate the signals that are unrelated to internal waves, the model used by C19 to simulate WaCM data is preferable to the model used by Wineteer et al. (2020). For applicability to actual future WaCM data, this assumes that internal wave variability can be adequately removed from the observations. As most of the internal wave variability that will be resolvable in the satellite data appears to be related to internal tides, it may be possible to suppress the internal wave signals by temporal averaging of the data. It remains to be determined whether the temporal sampling of a given location by WaCM, which consists of somewhat fewer than two samples per day in the California Current region considered here (see Fig. 10 in section 6 below), is sufficient to suppress the internal tide signals. An alternative approach that may be better is to remove the coherent components of internal tides using a deterministic model (e.g., Arbic 2022).

The analysis that follows begins with a brief summary in section 2 of the numerical model of the California Current System that is used to simulate WaCM data for this study. The statistical characteristics of the divergence and vorticity fields computed from the error-free surface velocity fields in the model are also summarized in section 2. The simulated WaCM measurements of surface currents are obtained from space-time sampling of the output of the model assuming a measurement footprint diameter of 5 km across a swath width of 1800 km with a nadir gap of 100 km centered on the satellite ground track. We consider only the effects of uncorrelated measurement errors (referred to herein interchangeably as measurement noise). The long-wavelength measurement errors that are neglected here have comparatively small effect on divergence and vorticity computed from WaCM measurements of surface currents because they are attenuated by the spatial high-pass filtering of the derivative operator.

A limitation of the analysis presented here is that the standard deviation of the uncorrelated errors in measurements of surface currents is assumed to be equally partitioned between the orthogonal along-track and across-track velocity components and to be spatially uniform across the 850-km measurement swath on each side of the nadir gap. In reality, the measurement errors will vary across the swaths because of limited azimuthal diversity of the multiple antenna viewing angles toward the edges of the swaths (see Fig. 13 of Rodríguez 2018). The noise of the along-track component of current velocity increases toward the outer edge of each swath, and the noise of the across-track component increases toward the inner edges. Because of the simplified modeling of measurement errors in this study, the conclusions about the effects of measurement noise on estimates of divergence and vorticity computed from simulated noisy WaCM data may be somewhat optimistic assessments of the resolution capabilities of actual future satellite estimates of divergence and vorticity.

The error characteristics of the ocean surface velocity components, divergence and vorticity with the above simplified characterizations of the measurement noise are discussed in section 3; analytical expressions for the standard deviations and wavenumber spectra of the noise for a footprint diameter of 5 km without and with additional spatial smoothing applied are given in appendices A and B. The noise of the velocity measurements with the 5-km footprint diameter of the simulated pre-processed data considered here is too large for the data to be useful in most applications without additional spatial smoothing and likely also temporal smoothing. The effects of spatial smoothing alone on the standard deviations and wavenumber spectral characteristics of the residual noise in estimates of surface velocity components, divergence and vorticity are summarized in section 3 for simulated pre-processed estimates of current velocity with speed noise standard deviations of $\sigma_{spd} = 0.25$, 0.15 and 0.05 m s^{-1}.

The procedure followed here to assess the resolution capabilities for estimates of divergence and vorticity from noisy satellite observations is summarized in section 4. Estimation of spatially smoothed instantaneous estimates of divergence and vorticity within a single measurement swath is then considered in section 5. In this case, the mapping errors consist mainly of the residual effects of measurement noise after the spatial smoothing. Artifacts can also occur near the swath edges and the coastal boundary in the form of sampling errors from edge effects of the spatial smoothing. The effects of temporal averaging of multiple swaths of data in an effort to further mitigate the effects of measurement noise are considered in section 6. Temporal averaging introduces an additional source of sampling errors from the undersampling of temporal variability of the divergence and vorticity fields, which evolve rapidly on the small submesoscales at which divergence and vorticity are most energetic. Since the analysis presented here is based on simulated data for which the error-free divergence and vorticity fields are known, the errors in estimates of divergence and vorticity can be partitioned between measurement noise and sampling errors to assess the relative importance of each source of error.

In the example maps of smoothed estimates of divergence and vorticity constructed from simulated noisy WaCM data that are presented here, the emphasis is on the case of a speed noise standard deviation of $\sigma_{spd} = 0.15$ m s^{-1} (see Figs. 7, 12, 14, and the bottom panels of Figs. 16 and 17 below). This noise level was chosen as a tradeoff between the need for high measurement accuracy for useful estimates of non-internal-wave contributions to divergence, and the practicality of what may be achievable from WaCM. From Fig. 2 of Wineteer et al. (2020), it appears that a speed noise standard deviation of $\sigma_{spd} = 0.15$ m s^{-1} is feasible over much of the measurement swath for conditions of wind speed greater than about 6 m s^{-1}. A measurement noise of $\sigma_{spd} = 0.15$ m s^{-1} is found to be too high for useful instantaneous snapshot estimates of divergence; a noise of $\sigma_{spd} = 0.05$ m s^{-1} is therefore used for the example maps in Fig. 6 below. On the other hand, it may be possible to relax the measurement accuracy requirement in regions where the divergence is stronger, larger in scale and more persistent. This is investigated in section 7 from a 31-day average of the divergence field within about 150 km of the California coast. It is shown in Figs. 16 and 17 below that it may be possible to obtain useful maps of the divergence associated with coastal upwelling in this region with a noise standard deviation of $\sigma_{spd} = 0.25$ m s^{-1} and temporal averages over 16 days.

2. The CCS model

The numerical model of the California Current System (CCS) used here to simulate WaCM measurements of surface ocean velocity is the same model that was used previously for the same purpose by C19. Detailed descriptions of the model can be found in Molemaker et al. (2015) and section 2 of C19. A brief summary is given here.

The computational code for the model was the Regional Oceanic Modeling System (ROMS), which solves the hydrostatic primitive equations for the velocity, potential temperature and salinity with a seawater equation of state. The model was configured for the CCS with open boundary conditions as the innermost of a sequence of three nested domains, all of which consisted of 40 stretched vertical levels with higher resolution near the surface. The largest-scale simulation spanned the full Pacific Ocean basin with a grid spacing that varied from 12.5 km at the central latitude of the model to 8.5 km at the northern and southern extremes near 55°N and 40°S. The model for the inner domain that is used for this study had a grid spacing of 0.5 km on a grid that was rotated by a polar angle of 24° so that the orthogonal x and y axes were aligned approximately across-shore and alongshore, respectively. The domain spans 600 km in the across-shore dimension and 900 km in the alongshore dimension, extending from Point Conception in the south to approximately the California/Oregon border in the north. For the analysis presented in this study, we consider only the 31-day time period from day 141 to day 171, which corresponds to 21 May through 20 June during which submesoscale variability is fully developed in the CCS region. The model output during this time period was subsampled at intervals of 0.5 days.

It is noteworthy that the ROMS model is based on a terrain-following vertical grid. The CCS model used in this study has 40 levels, regardless of the water depth. The depth of the uppermost level thus decreases by more than a factor of 10 from O(10) m in deep water to O(1) m over the continental shelf, which has a width of about 50 km in the CCS region considered here. The potentially important issue of how the geographical variation of the thickness of the upper level affects the interpretation of the upper-level velocity as “surface velocity" is not not addressed in this study.

The model was forced by the seasonal cycle of wind stress based on the Scatterometer Climatology of Ocean Winds (Risien and Chelton 2008), and seasonal cycles of heat and freshwater fluxes from the Comprehensive Ocean-Atmosphere Data Set (Da Silva et al. 1994). Because high-frequency variability is not included in the forcing, inertial motions are poorly represented in the model. In addition, the model had high dissipation and did not include ocean tidal forcing. Internal gravity waves are therefore much weaker in the model than in the real ocean. For the purpose of this study, which is interested only in the non-internal-wave contributions to the divergence and vorticity of surface currents, the weak internal wave energy is advantageous. The applicability of the results to actual WaCM data will require removal of the internal wave signals. The question of how that can be achieved in practice is not addressed here.

A representative map of the early summertime speed of surface currents in the CCS region is shown in Fig. 1a. The ribbon of fast surface flow that separates from the near-coastal region at Cape Blanco just north of the model domain is the meandering equatorward California Current. Submesoscale variability is highly energetic within and inshore of the core of the current. While submesoscale variability also exists in the offshore region, the variability becomes more dominated by mesoscale features.

Vorticity and divergence were computed from the gridded fields of the u and v components of surface ocean velocity by approximating the derivatives using 3-point centered differences on the 0.5 km $\times$ 0.5 km model grid. The resulting estimates of vorticity and divergence normalized by the local Coriolis parameter f at each grid point are shown in Figs. 1b and c, respectively. Note the smaller dynamic range of the color bar for the divergence map, indicative of the weaker signals in divergence compared with vorticity. The rich submesoscale variability is much more apparent in both vorticity and divergence than in ocean velocity because of the spatial high-pass filtering operation of the centered difference approximation of the derivatives that emphasizes small-scale features.

The scale dependences of the vorticity and divergence are quantified in Figs. 2a and b, which show the probability distributions of each variable determined by isotropic smoothing of the maps in the upper panels of Figs. 1b and c using a Parzen smoother (see appendix A of C19) with

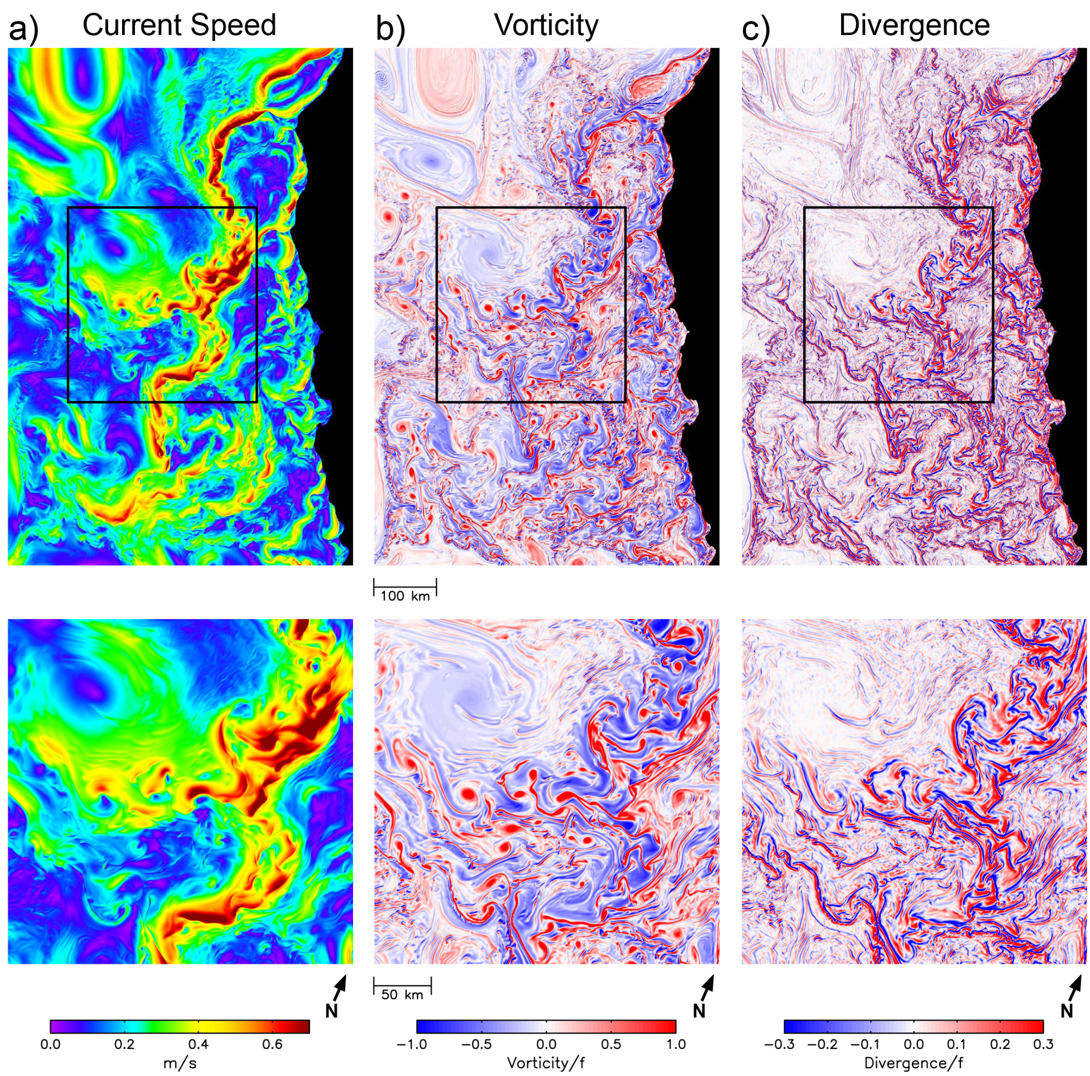

FIG. 1. Representative summertime snapshot maps from the ROMS model of the CCS on 5 June at the full 0.5 km × 0.5 km grid resolution of the model: Column (a) the speed of the total surface velocity; Column (b) the normalized vorticity ζ/f computed from the surface velocity, where f is the local Coriolis parameter at each grid point; and Column (c) the normalized divergence δ/f computed from the surface velocity. The bottom panels are enlargements of the region delineated by the box in each of the top panels. For reference, a divergence of $\delta/f = 0.3$ at the central latitude 37°N of the model corresponds to a vertical velocity of about 11.4 m day^{-1} when integrated to a depth of 5 m. The x, y coordinate system of the model is rotated by a polar angle of 24° relative to longitude-latitude coordinates. An unrotated map of the model domain in longitude-latitude coordinates is shown in Fig. 9 below.

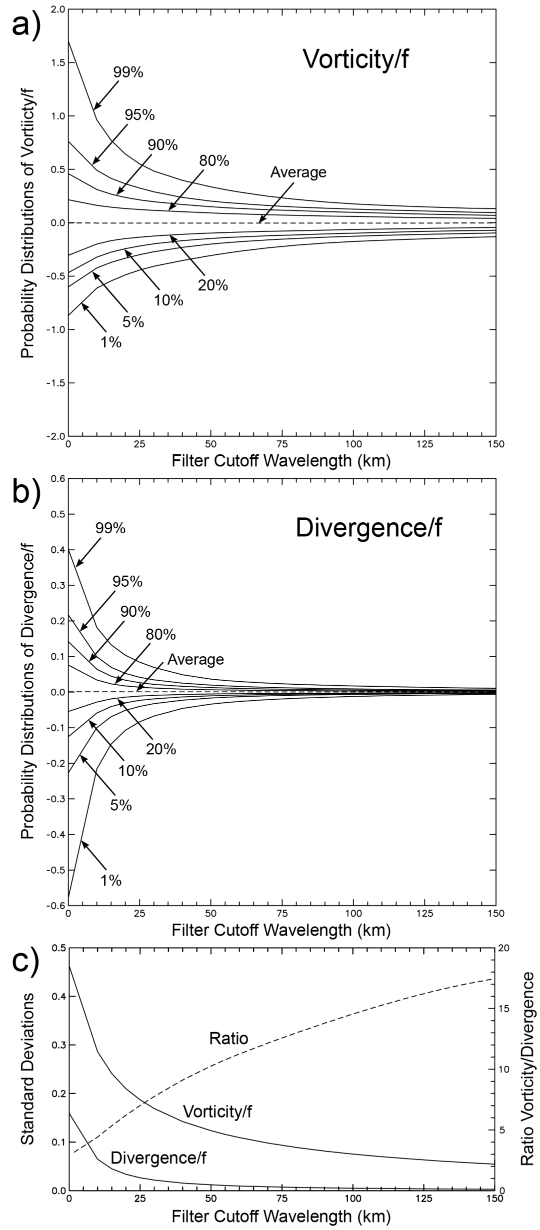

FIG. 2. The scale dependences of selected percentage points symmetric about the median (i.e., the 50th percentile point) in the distributions of (a) normalized vorticity ζ/f; and (b) normalized divergence δ/f as functions of half-power filter cutoff wavelength. The standard deviations of ζ/f and δ/f and their ratio (dashed line) are shown in (c). For all panels, ζ and δ were computed from error-free model fields of surface velocity at the full 0.5 km $\times$ 0.5 km grid resolution of the model after smoothing with the half-power filter cutoff wavelengths indicated along the abscissa.

successively longer half-power filter cutoff wavelengths from 0 to 150 km. To avoid problems with edge effects of the smoothing, the areas of the CCS model grid within 50 km of the northern, western and southern boundaries were excluded from the calculations of the percentage points of the distributions. The distributions of both variables are asymmetric at small scales; divergence is skewed toward negative values (convergence) and the vorticity is skewed toward positive values (cyclonic variability).

The dynamic range of the ordinate for the distribution of divergence in Fig. 2b is smaller by about a factor of 3 than the ordinate for the distribution of vorticity in Fig. 2a. In addition to divergence being much smaller in magnitude than vorticity on all scales, it decreases in magnitude much more quickly with increasing scale. This is consistent with the strong tendency for ocean currents to be quasi-geostrophic on the larger scales. The relative magnitudes of divergence and vorticity are characterized in Fig. 2c by their standard deviations as a function of spatial scale. The ratio of the standard deviations of vorticity to divergence shown by the dashed line is about 3 at the smallest scales resolvable by the 0.5 km × 5 km grid and increases monotonically to about 17 at the largest scale of 150 km considered in Fig. 2.

3. The error characteristics of velocity, divergence and vorticity

To simulate WaCM data, the 0.5 km × 0.5 km output of the CCS model summarized in section 2 was smoothed isotropically with a half-power filter cutoff wavelength of 10 km. This yields velocity estimates with a footprint diameter of 5 km (see appendix B of C19). The 10-km smoothed velocity fields from the model were then subsampled within two parallel measurement swaths in simulated overpasses of WaCM. Each of the two swaths had a width of 850 km and were separated by a 100-km gap centered on the satellite ground track, thus resulting in a full span of 1800 km. It was assumed that the speed noise is equally partitioned between the u and v components. The standard deviation of the noise in each velocity component is then

$$\sigma_{u,v} = \frac{\sigma_{spd}}{\sqrt{2}}. \tag{1}$$

For the case of a speed measurement noise of $\sigma_{spd} = 0.25$ m s^{-1}, for example, the noise of each velocity component is $\sigma_{u,v} = 0.177$ m s^{-1}. Gaussian distributed random errors were added to the 10-km smoothed values of each velocity component with spatially homogeneous speed noise standard deviations σ_{spd} ranging from 0.05 m s^{-1} to 0.50 m s^{-1} in increments of 0.05 m s^{-1}.

As discussed in the introduction, the noise in WaCM measurements of each velocity component will vary in different ways across the measurement swaths. The simplified assumptions of a spatially homogeneous noise standard deviation and equal partitioning of the measurement errors between u and v that are assumed here imply that the resolution capabilities inferred for divergence and vorticity from the analysis in sections 5–7 is likely optimistic, especially toward the inner and outer edges of the swaths where the assumption of equal partitioning of the velocity component errors becomes progressively less valid. The analysis presented here nonetheless provides a useful understanding of the effects of velocity measurement noise on estimates of divergence and vorticity obtained from WaCM data.

Analytical expressions for the standard deviations of the noise in WaCM estimates of divergence and vorticity are given in appendix A. For a speed noise standard deviation of $\sigma_{spd} = 0.25$ m s^{-1}, for example, it is shown that the noise in divergence and vorticity is $1.22 f_{37°\mathrm{N}}$, where $f_{37°\mathrm{N}} = 8.8 \times 10^{-5}$ s^{-1} is the Coriolis parameter at the center latitude of the CCS model considered here. With errors this large, applications of vorticity and divergence estimated from WaCM data with a footprint diameter of 5 km will clearly require additional smoothing to reduce the effects of measurement errors.

To facilitate the discussion that follows, the simulated WaCM measurements of current velocity with the footprint diameter of 5 km that will be obtained in pre-processing onboard the satellite by isotropic smoothing of the raw data with a half-power filter cutoff wavelength of 10 km will be referred to hereinafter as “unsmoothed" in order to distinguish them from the velocity fields that will obtained in ground-based post-processing by applying additional smoothing to the data.

The dependence of the standard deviation $\overline{\sigma}_{u,v}$ of the residual noise in the velocity component fields after smoothing in post-processing was determined empirically by generating simulated fields of uncorrelated velocity component noise on the CCS model grid and smoothing isotropically using Parzen smoothers with half-power filter cutoff wavelengths ranging from $\lambda_c = 10$ to 150 km. The results are shown in Fig. 3a for the cases of unsmoothed velocity component noise (1) with speed standard deviations of $\sigma_{spd} = 0.50$, 0.25 and 0.10 m s^{-1} (thick, medium and thin lines, respectively).

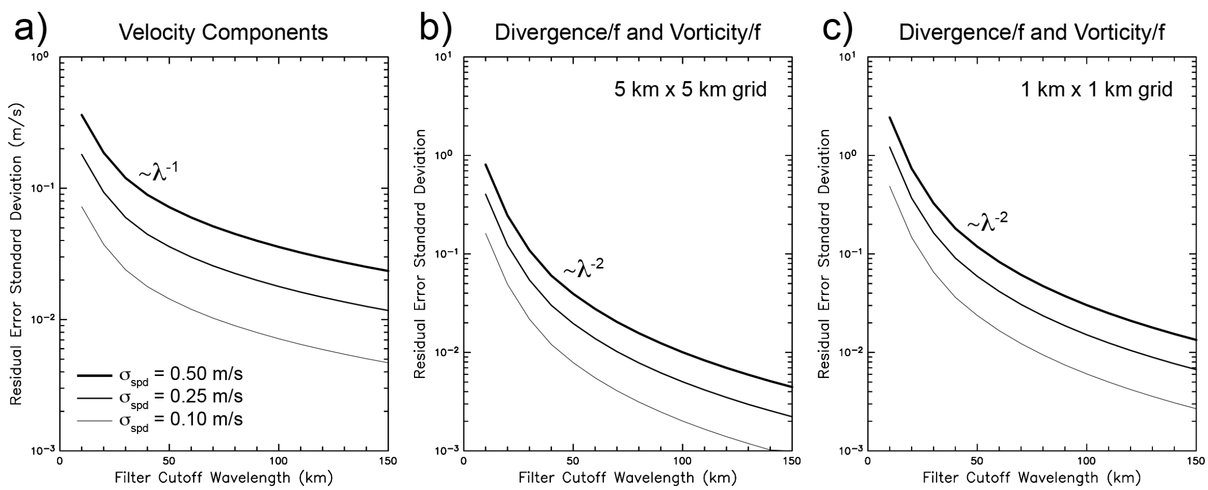

FIG. 3. The standard deviations of residual noise as functions of half-power filter cutoff wavelength λ_c for isotropic 2-dimensional smoothing of simulated WaCM data using Parzen smoothers for the cases of speed noise standard deviations of $\sigma_{spd} = 0.50$, 0.25 and 0.10 m s^{-1} (thick, medium and thin lines, respectively): a) velocity component estimates; b) divergence and vorticity computed from the velocity components on a 5 km × 5 km grid and normalized by the Coriolis parameter $f_{37^\circ\mathrm{N}} = 8.8 \times 10^{-5}$ s^{-1} at the center latitude 37°N of the CCS model domain; and c) divergence and vorticity computed from the velocity components on an oversampled 1 km × 1 km grid and normalized by $f_{37^\circ\mathrm{N}}$.

It can be seen from Fig. 3a that $\overline{\sigma}_{u,v}$ has a λ_c^{-1} dependence on the filter cutoff wavelength. This dependence can be derived analytically from Eq. (D.5a) in appendix D of C19 that shows that the residual noise variance $\overline{\sigma}^2_{u,v}$ of smoothed velocity component fields is proportional to the variance $\sigma^2_{u,v}$ of the unsmoothed velocity components with a proportionality constant α that depends according to Eq. (D.5b) on the filter transfer function of the particular choice of smoother applied to the data. For isotropic smoothing with the Parzen smoother used here, α is given by Eq. (D.14c) of C19, which can be expressed in the form $\alpha = 4d^2\lambda_c^{-2}$, where $d = 5$ km is the footprint diameter of the pre-processed WaCM measurements of surface currents. The proportionality constant is similar for other smoothing algorithms if the parameters of the smoother are chosen to give the same filter cutoff wavelength λ_c. For any choice of smoothing, the standard deviation of the residual noise after smoothing is thus given approximately by

$$\overline{\sigma}_{u,v} = 10\sigma_{u,v}\lambda_c^{-1} = \frac{10\sigma_{spd}}{\sqrt{2}}\lambda_c^{-1}. \qquad (2)$$

For the cases of $\sigma_{spd} = 0.50$, 0.25 and 0.10 m s^{-1} shown in Fig. 3a, (2) becomes $\overline{\sigma}_{u,v} = 3.54\lambda_c^{-1}$, $1.77\lambda_c^{-1}$ and $0.708\lambda_c^{-1}$, respectively. These analytical solutions are indistinguishable from the residual noise standard deviations in Fig. 3a that were computed empirically from the simulated noise fields.

For the footprint diameter of 5 km assumed here for the pre-processed estimates of current velocity, the noise in the velocity component estimates is uncorrelated on a 5 km × 5 km sample grid (see appendix B of C19). It is advantageous to oversample the velocity estimates on a 1 km × 1 km grid because the wavenumber filter response function of the 3-point centered difference approximations of derivatives retains more of the high-wavenumber variability in the vorticity and divergence signals (see appendix H of C19). This becomes more and more advantageous with decreasing noise standard deviation σ_{spd}. For the analysis presented here, it is assumed that the WaCM data will be available on a 1 km × 1 km grid.

The dependence of the standard deviations $\sigma_{\zeta,\delta}$ of unsmoothed divergence and vorticity noise depends on the grid spacing of the estimates according to (A2) and (A5). The standard deviations $\overline{\sigma}_{\zeta,\delta}$ of the smoothed fields likewise also depend on the grid spacing of the estimates. The dependences of $\overline{\sigma}_{\zeta,\delta}$ on the filter cutoff wavelength λ_c are shown normalized by $f_{37°\mathrm{N}}$ for grid spacings of 5 km and 1 km in Figs. 3b and c, respectively, for the cases of unsmoothed velocity component noise (1) with speed standard deviations of $\sigma_{spd} = 0.50$, 0.25 and 0.10 m s^{-1}. The decreases with increased smoothing can be very closely approximated by power-law dependences on λ_c of the form

$$\frac{\overline{\sigma}_{\zeta,\delta}}{f_{37°\mathrm{N}}} = \hat{a}\lambda_c^{-2}. \tag{3}$$

For latitudes other than 37°N, the value of the normalized standard deviations of the residual errors shown in Figs. 3b and c must be multiplied by $(f_{37°\mathrm{N}}/f)$, where f is the Coriolis parameter at the latitude of interest.

The coefficient $\hat{a}$ in (3) depends on the speed noise standard deviation σ_{spd} of the unsmoothed measurement noise and the grid spacing of the divergence and vorticity estimates. For the case of $\sigma_{spd} = 0.50$ m s^{-1} on the oversampled grid spacing of 1 km (the thick line in Fig. 3c), the regression estimate of $\hat{a}$ for wavelengths longer than 25 km is 294.6 km^3. This coefficient scales proportionally with σ_{spd} and thus decreases to 147.3 and 58.92 km^3 for $\sigma_{spd} = 0.25$ and 0.10 m s^{-1}, respectively (the medium and thin lines in Fig. 3c).

Commensurate with the differences between (A7) and (A4), the coefficient $\hat{a}$ for smoothed divergence and vorticity noise on a 5-km grid that is shown in Fig. 3b is a factor of 3 smaller than its counterpart for the oversampled 1-km grid shown in Fig. 3c. It should be noted that the regression estimates do not fit the empirically computed standard deviations $\overline{\sigma}_{\zeta,\delta}$ in Fig. 3 quite as well at wavelengths shorter than about 25 km because of the double smoothing of the noise. The contribution of the smoothing of the raw data with a filter cutoff wavelength of 10 km in the pre-processing to simulate measurements with a footprint diameter of 5 km decreases rapidly in importance compared with the application of additional smoothing in post-processing, becoming negligible for filter cutoff wavelengths λ_c larger than 20 km.

Analytical expressions for the wavenumber spectra of the noise in WaCM estimates of divergence and vorticity are given in appendix B. For the case of a uniform 1 km × 1 km grid spacing and equal partitioning (1) of the measurement noise between the u and v components, the wavenumber spectra of the noise in divergence and vorticity are exactly the same. The resulting analytical expression is shown by the green lines in the top panels of Fig. 4 for measurement noise with speed standard deviations of $\sigma_{spd} = 0.50$, 0.25 and 0.10 m s^{-1} (left to right). The somewhat noisy pair of blue lines in each panel are the spectra of divergence and vorticity noise computed empirically from the simulated fields of WaCM measurement noise. The two empirical noise spectra and the analytical spectrum in each panel are difficult to distinguish, thus validating the analytical solutions (B1) and (B3) for the noise spectrum.

For comparison, the signal spectra of divergence and vorticity from the CCS model smoothed 10 km to simulate error-free WaCM data with a footprint diameter of 5 km are shown in the top three panels of Fig. 4 by the thick and thin red lines, respectively, which are the same in all three panels. The spectra computed from the 0.5 km × 0.5 km gridded output of the model without 10-km smoothing are shown by the black lines in the upper left panel of Fig. 4. The spectra of the vorticity signals are redder (more dominated by low frequencies) than those of the divergence signals, and are much more energetic over all frequencies. At all wavenumbers, the noise spectra are more than an order of magnitude more energetic than the vorticity signal spectrum, and more than two orders of magnitude more energetic than the divergence signal spectrum. This again underscores the need for additional smoothing of the WaCM data in ground-based post-processing.

Analytical expressions are also given in appendix B for the wavenumber spectra of the noise in smoothed divergence and vorticity computed from smoothed velocity component errors. The spectra of noise in divergence and vorticity are again the same for smoothed fields for the uniform grid spacing and equal partitioning of the measurement noise between the two components assumed here. The resulting analytical expression is shown by the green lines in the bottom nine panels of Fig. 4 for speed noise standard deviations of $\sigma_{spd} = 0.50$, 0.25 and 0.10 m s^{-1} (left to right) and half-power filter cutoff wavelengths of $\lambda_c = 50$, 100 and 150 km (second, third and fourth rows, respectively). The somewhat noisy pair of blue lines in each panel are the spectra of smoothed

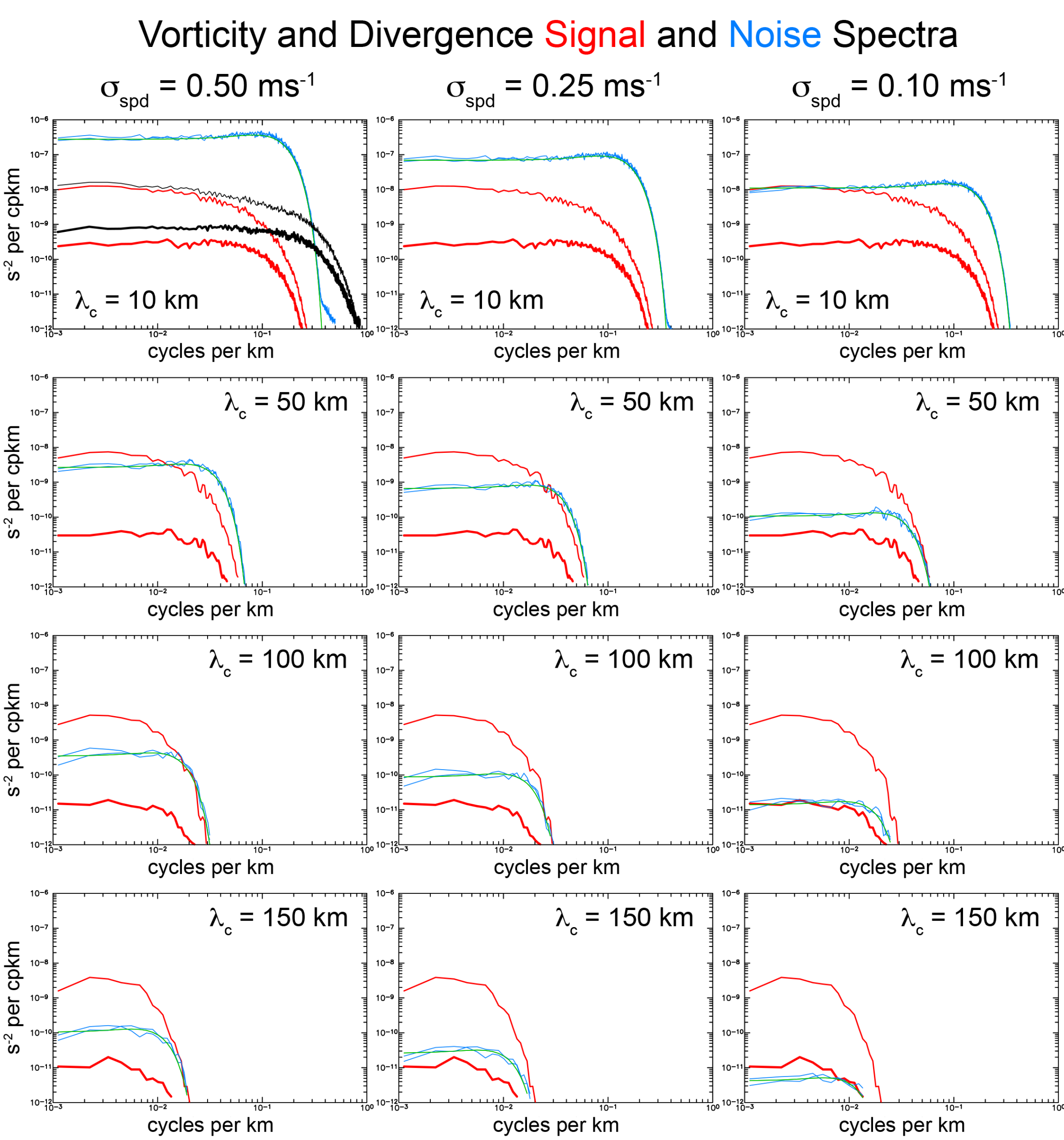

FIG. 4. Along-track wavenumber spectra of the noise of divergence and vorticity computed from velocity measurement noise with speed standard deviations of σ_{spd} = 0.50, 0.25 and 0.10 m s^{-1} (left to right). The green lines are the analytical solutions for the noise spectra (see appendix B) and the two blue lines in each panel are the noise spectra computed empirically from simulated fields of divergence and vorticity noise computed from velocity component noise. The panels in the top row are for "unsmoothed" simulated WaCM data with a footprint diameter of 5 km, which are computed in onboard pre-processing by smoothing the raw data with a half-power filter cutoff wavelength of 10 km. The panels in each of the lower three rows are for data smoothed isotropically in post-processing using a Parzen smoother with half-power filter cutoff wavelengths of λ_c = 50, 100 and 150 km (second, third and fourth rows, respectively). The red lines are the divergence and vorticity signal spectra (thick and thin lines, respectively, which are the same in all three panels in each row) smoothed in the same manner as the noise. The black lines in the top left panel are the divergence and vorticity signal spectra computed from the CCS model on the 0.5 km × 0.5 km model grid without the 10-km smoothing in simulated pre-processing to achieve a footprint diameter of 5 km.

divergence and vorticity noise computed empirically from the simulated fields of smoothed WaCM measurement noise. The two empirical noise spectra and the analytical spectrum in each panel are again difficult to distinguish, thus validating the analytical solutions (B4) and (B5) for the spectra of smoothed noise.

The signal spectra of divergence and vorticity from the CCS model smoothed with the same filter cutoff wavelength λ_c as the noise are shown in Fig. 4 by the thick and thin red lines, respectively. For all three choices of measurement noise standard deviation σ_{spd} and all three filter cutoff wavelengths λ_c, the spectra of smoothed vorticity exceed the noise spectra, albeit barely for the case of large measurement noise σ_{spd} = 0.50 m s^{-1} and small spatial smoothing with λ_c = 50 km. For divergence, however, the smoothed signal spectrum only exceeds the noise spectrum for the case of a small measurement noise of σ_{spd} = 0.10 m s^{-1} and large spatial smoothing with λ_c = 150 km. Estimation of divergence with the magnitudes represented in the CCS model used here will clearly be a major challenge for Doppler scatterometry.

4. The procedure for assessing resolution capability

The procedure followed in this study to assess the resolution capability of divergence and vorticity fields estimated from noisy WaCM data is described in detail in section 5 of C19. A brief summary is given here. The approach taken is to determine from simulated data how much smoothing is required to achieve a specified signal-to-noise ratio (S/N) that is determined from the spatial standard deviations of the residual error-free signals and the residual errors after smoothing. For the case of spatial smoothing alone in the instantaneous snapshots of noisy fields that are considered in section 5, the errors consist almost entirely of measurement noise. If the smoothing includes temporal averaging as in sections 6 and 7, the total error also includes errors that arise from the limited swath width of WaCM measurements and by the fact that the discrete and irregular temporal sampling does not fully resolve the rapidly evolving submesoscale signals at a given location. These sampling errors would occur even if the measurements themselves were error-free.

The smoothing applied to noisy estimates of a variable in order to attenuate the effects of measurement and sampling errors also attenuates the signals that are of interest. The error variance generally decreases more rapidly than the signal variance, albeit less so for divergence than for vorticity because divergence is less energetic and more dominated by small-scale variability. The resolution capability is defined here to be the half-power filter cutoff wavelength λ_c above which the S/N standard deviation ratios γ exceed a specified threshold.

The choice of the threshold value of γ for defining resolution capability is inevitably subjective. S/N standard deviation ratios of 1.00, 2.00 and 3.16 (corresponding to variance ratios of 1, 4 and 10) were considered by C19. From visual inspection of example noisy fields with these three choices of γ (see Fig. 16 of C19), C19 advocate the use of a threshold criterion of $\gamma = 3.16$, arguing that a smaller value of $\gamma = 2.00$ is insufficient to distinguish the signal from the errors unambiguously. This can also be seen from Figs. 6 and 7 below.

It is shown in section 5 of C19 that values of $\gamma = 3.16$ and 2.00 correspond to correlations of 0.95 and 0.89, respectively, between the smoothed error-free field and the smoothed field constructed from simulated observations with measurement noise and sampling errors. The choice of $\gamma = 3.16$ may seem overly conservative to some readers. The resolution capabilities for WaCM estimates of divergence and vorticity that are presented in sections 5–7 are shown in Fig. 8 below for threshold ratios γ of 3.16 and 2.00 to allow user discretion in the choice of the threshold criterion for γ.

5. The effects of measurement noise in instantaneous snapshots

The resolution capabilities of snapshots of divergence and vorticity computed from WaCM data are considered in this section by determining the S/N standard deviation ratio γ after applying isotropic 2-dimensional spatial smoothing to simulated measurements within one of the two 850-km measurement swaths for a single ascending overpass of the CCS model domain (see the left panel of Fig. 9 below). The errors in the smoothed fields constructed in this manner consist predominantly of measurement noise. However, sampling errors cannot be totally avoided because of artifacts that can occur in smoothed estimates of divergence and vorticity near the edges of the measurement swaths and coastline. These edge effects arise from incomplete data within the span of the 2-dimensional smoother. Technically, estimates at locations within half the smoothing span of a swath edge or coastline are imperfect. In practice, useful estimates can be obtained much closer than this to a swath edge or coastline. This is because smoothers weight the data near the estimation location much more heavily than the data near the outer edge of the smoother. It is shown in section 5 of Chelton et al. (2022) that 98% of the weighting of the Parzen smoother that is used throughout this study lies within a radial distance of $\lambda_c/3$ from the estimation location, where λ_c is the half-power filter cutoff wavelength of the smoother. For the case of $\lambda_c = 100$ km, for example, edge effects are usually a concern only within 25 or 30 km of the swath edge or coastline.

The analysis in this section is based on simulated WaCM measurements of surface current velocity with a footprint diameter of 5 km on an oversampled 1-km grid. Uncorrelated noise equally partitioned between the u and v components was added to the velocity estimates obtained from the model. For each choice of the speed noise standard deviation σ_{spd} that was considered, the resolution capabilities for divergence and vorticity were assessed from the S/N standard deviation ratios by applying the same smoothing to the error-free and noisy fields for half-power filter cutoff wavelengths ranging from $\lambda_c = 10$ km to 200 km. The results are shown in Fig. 5 for $\sigma_{spd} = 0.25$, 0.15 and 0.05 m s^{-1}.

The challenge for estimation of divergence is readily apparent from the fact that the S/N standard deviation ratios for the cases of $\sigma_{spd} = 0.25$ or 0.15 m s^{-1} in the top and middle panels of Fig. 5 do not even reach the liberal threshold criterion of $\gamma = 2.00$ for the range of filter cutoff wavelengths shown in the graphs. For a measurement noise of $\sigma_{spd} = 0.05$ m s^{-1}, which seems highly optimistic for Doppler scatterometry, the resolution capabilities for divergence based on threshold criteria

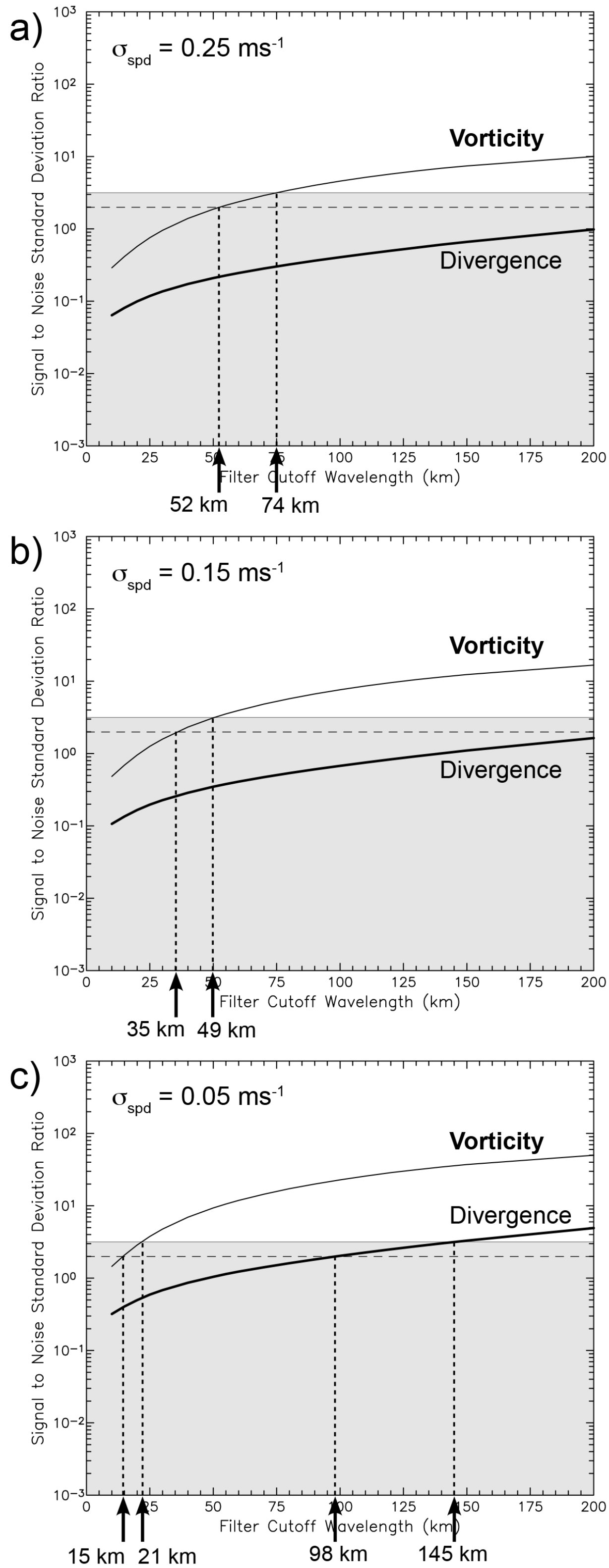
a)
σspd = 0.25 ms-1
Vorticity
Divergence
Signal to Noise Standard Deviation Ratio
Filter Cutoff Wavelength (km)
52 km
74 km
b)
σspd = 0.15 ms-1
Vorticity
Divergence
Signal to Noise Standard Deviation Ratio
Filter Cutoff Wavelength (km)
35 km
49 km
c)
σspd = 0.05 ms-1
Vorticity
Divergence
Signal to Noise Standard Deviation Ratio
Filter Cutoff Wavelength (km)
15 km
21 km
98 km
145 km

FIG. 5. The scale dependences of the ratios of the standard deviations of smoothed signal and errors for a snapshot of the full CCS region for WaCM estimates of instantaneous divergence and vorticity (thick and thin lines, respectively) after isotropic 2-dimensional smoothing using Parzen smoothers with the half-power filter cutoff wavelengths indicated along the abscissas for speed noise standard deviations of $\sigma_{spd} = 0.25$, 0.15 and 0.05 m s^{-1} (top to bottom). The gray areas correspond to S/N standard deviation ratios lower than 3.16. The horizontal dashed line in each panel corresponds to S/N=2.00. The vertical dashed lines indicate the filter cutoff wavelengths at which the S/N ratios are 2.00 and 3.16. The resolution capabilities for divergence estimates with speed noise standard deviations of $\sigma_{spd} = 0.25$ and 0.15 m s^{-1} are coarser than the maximum value of 200 km on the abscissas.

of $\gamma = 3.16$ and 2.00 are about $\lambda_c = 145$ and 100 km, respectively. Smoothed maps of noisy and error-free estimates of divergence for a speed noise standard deviation of $\sigma_{spd} = 0.05$ m s^{-1} are shown in Fig. 6 for these two choices of λ_c. In the upper left panel of Fig. 6 for which $\gamma = 2.00$, there are many small-scale features that are artifacts of noise but could easily be mistaken for small-scale eddies. There are far fewer such features in the bottom left panel for which $\gamma = 3.16$. In the discussion that follows, the resolution capability will be defined as in C19 by the threshold criterion of $\gamma = 3.16$.

The existence of edge effects is readily apparent near the upper left corner of the maps in the left and right columns of Fig. 6. The black triangular area at the upper left corner is part of the nadir gap between the two parallel 850-km measurement swaths (see Fig. 9 below). Not surprisingly, these edge effects do not extend as far into the measurement swath for the 100-km smoothing in the top panels as for the 145-km smoothing in the bottom panels. In the case of the latter, the edge effects appear visually to be restricted to the area within about 40 km of the swath edge. This is consistent with the discussion above of the concentration of 98% of the weighting function of the Parzen smoother within a distance of about $\lambda_c/3$ of the estimation location. Although not visually apparent, some of the divergence field near the coastline is likely also contaminated to some degree by edge effects for the 145-km smoothing applied in the bottom panels of Fig. 6.

It is much easier to estimate vorticity than divergence from WaCM data. Moreover, estimates of vorticity are much less sensitive to measurement noise than was the case for estimates of divergence. As shown in Fig. 5, the resolution capability according to the threshold criterion of $\gamma = 3.16$ is about 75 km for $\sigma_{spd} = 0.25$ m s^{-1} and improves to about 50 km for $\sigma_{spd} = 0.15$ m s^{-1} and 20 km for

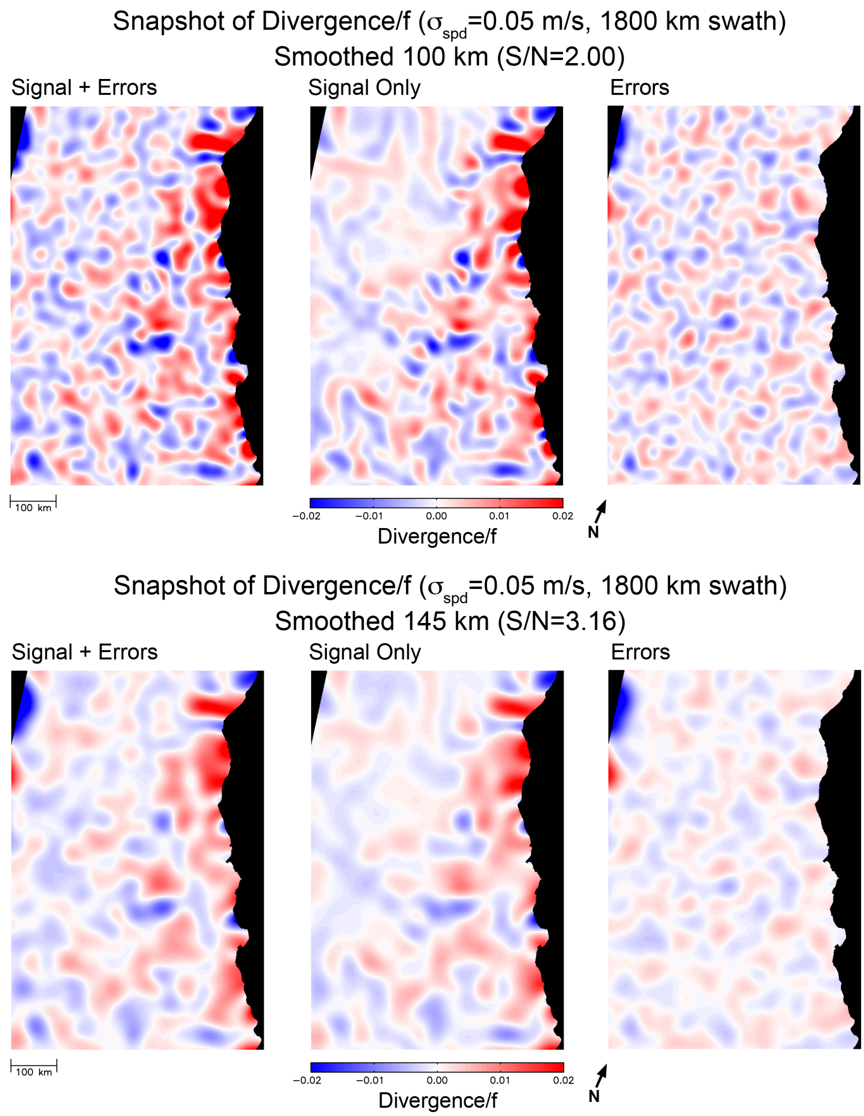

FIG. 6. Representative snapshot maps of noisy (left panels) and error-free (middle panels) divergence and the associated errors (right panels) computed from simulated WaCM measurements of surface velocity with a highly optimistic speed noise standard deviation of $\sigma_{spd} = 0.05$ m s^{-1} that is required for useful snapshot estimates of divergence. The signal and noise were smoothed using Parzen smoothers with half-power filter cutoff wavelengths of $\lambda_c = 100$ and 145 km (top and bottom, respectively), which correspond to S/N standard deviation ratios of approximately 2.00 and 3.16 (see Fig. 5c). For reference, a divergence of $\delta/f = 0.02$ at the central latitude 37°N of the model corresponds to a vertical velocity of about 0.76 m day^{-1} when integrated to a depth of 5 m.

$\sigma_{spd} = 0.05$ m s^{-1}. A noise of $\sigma_{spd} = 0.05$ m s^{-1} seems unrealistically optimistic, except possibly in very high-wind conditions (see Fig. 2 of Wineteer et al. 2020). Maps for a more realistic goal of $\sigma_{spd} = 0.15$ m s^{-1} are shown in Fig. 7 for the filter cutoff wavelengths of 35 and 50 km that correspond to S/N ratios of $\gamma = 2.00$ and 3.16, respectively. Note that there are no apparent edge

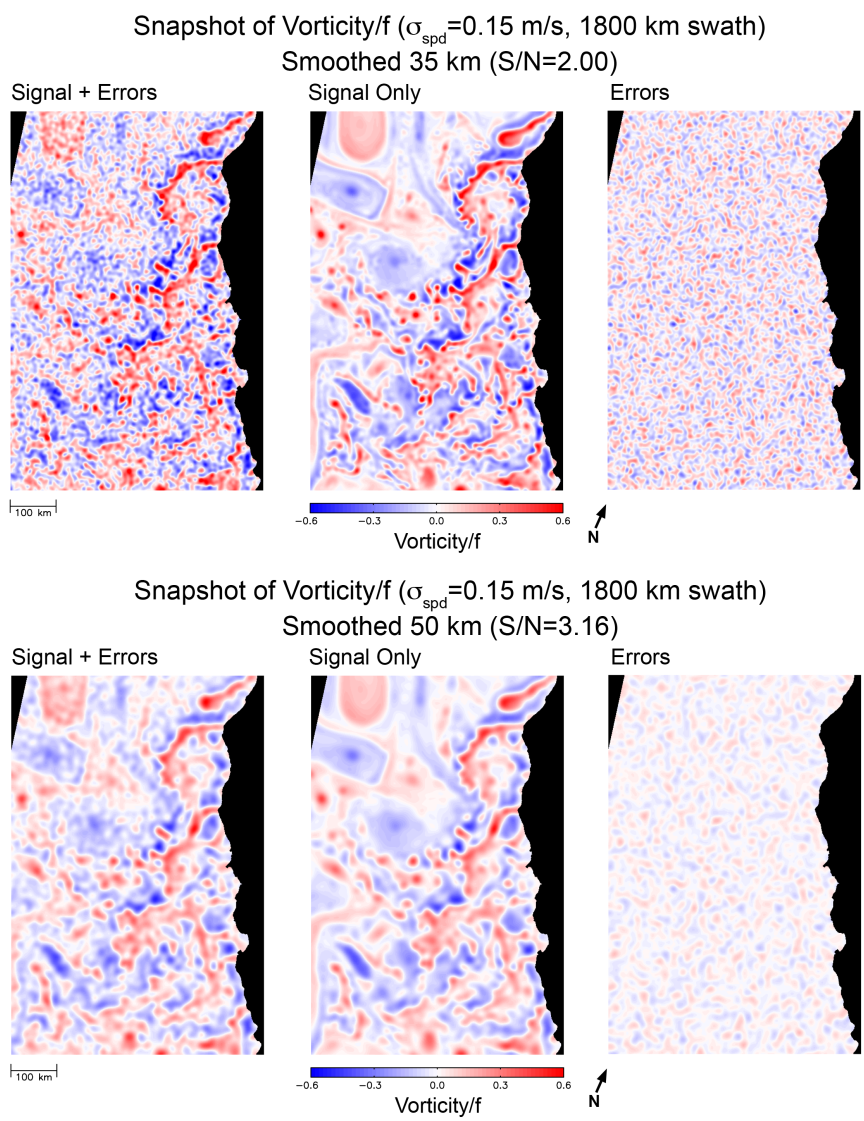

FIG. 7. Representative snapshot maps of noisy (left panels) error-free (middle panels) vorticity and the associated errors (right panels) computed from simulated WaCM measurements of surface velocity with a speed noise standard deviation of $\sigma_{spd} = 0.15$ m s^{-1}. The signal and noise were smoothed using Parzen smoothers with half-power filter cutoff wavelengths of $\lambda_c = 35$ and 50 km (top and bottom, respectively), which correspond to S/N standard deviation ratios of approximately 2.00 and 3.16 (see Fig. 5b).

effects in these maps because the filter cutoff wavelengths are much shorter than those that were necessary for the smoothed maps of divergence in Fig. 6. As in the case of divergence, there are many small-scale features in the upper left panel of Fig. 7 for which $\gamma = 2.00$ that are artifacts of noise but could easily be mistaken for small-scale eddies, thus underscoring again the inadequacy of a threshold S/N ratio criterion of $\gamma = 2.00$ for defining resolution capability.

The procedure used to generate the graphs in Fig. 5 was applied for speed noise standard deviations σ_{spd} ranging from 0.05 to 0.50 m s^{-1}. The resolution capabilities defined by threshold S/N standard deviation ratios of $\gamma = 3.16$ and 2.00 are summarized graphically in the top two panels of Fig. 8 by the solid and dashed lines, respectively, for WaCM estimates of snapshots of divergence and vorticity. The resolution capabilities for divergence with speed noise standard deviations larger than $\sigma_{spd} = 0.15$ m s^{-1} for the case of $\gamma = 3.16$ and larger than $\sigma_{spd} = 0.20$ m s^{-1} for the case of $\gamma = 2.00$ are coarser than the extreme plotted values of λ_c displayed in the figure.

6. The effects of combined measurement noise and sampling errors in 4-day and 16-day averages

For the snapshots of WaCM estimates of divergence and vorticity within a single measurement swath that were considered in section 5, the only option for attenuating the effects of measurement noise was to apply 2-dimensional spatial smoothing to the data. The effects of measurement errors can be further suppressed by considering multiple swaths of data and averaging over time. Moreover, temporal averaging will be necessary for mapping divergence and vorticity fields over a domain larger than a single measurement swath. Time averaging of measurements from multiple swaths can introduce additional artifacts from sampling errors that would occur even if the measurements were error-free. These sampling errors arise from the fact that the measurements at discrete times do not fully resolve the rapidly evolving and energetic submesoscale variability that is much more pronounced in divergence and vorticity than in velocity (see Fig. 1). The various manifestations of sampling errors are discussed in detail in section 7 of C19. Unfortunately, time averaging also attenuates the divergence and vorticity signals that are of interest. The question addressed in this section is whether time averaging significantly improves the signal-to-noise ratio, where “noise" now includes sampling errors as well as the uncorrelated measurement errors considered in section 5.

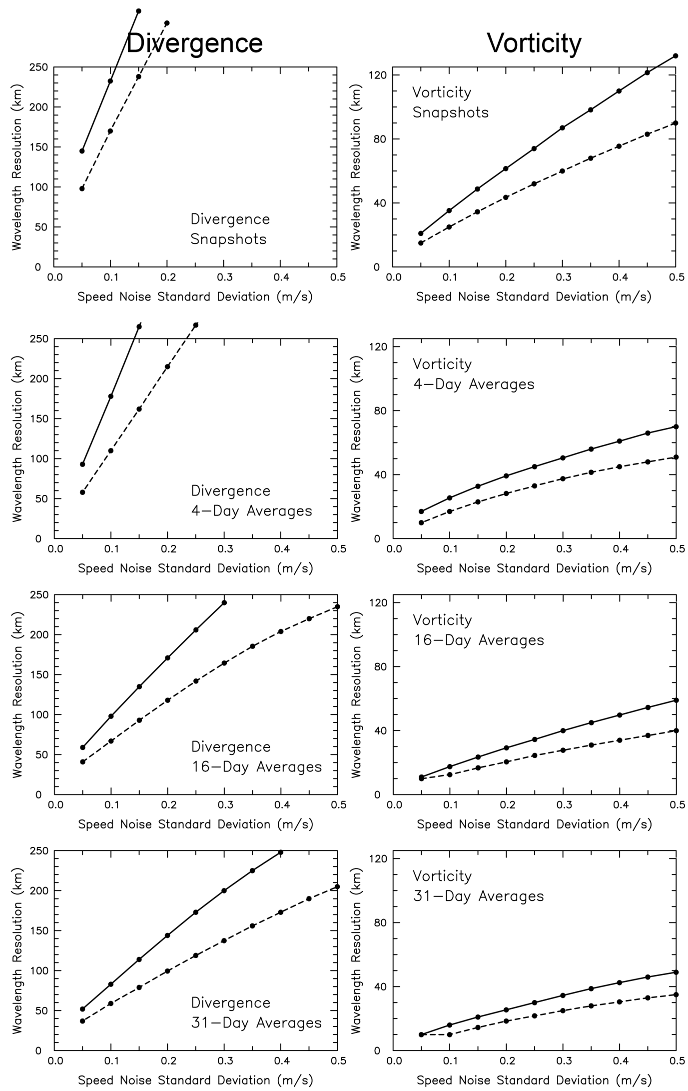

FIG. 8. The resolution capabilities of WaCM estimates of divergence (left column) and vorticity (right column) as functions of the standard deviation σ_{spd} of the velocity measurement noise. Note the larger dynamic range of the ordinates in the graphs for divergence. The solid and dashed lines correspond to the resolution capabilities inferred from threshold S/N standard deviation ratios of 3.16 and 2.00, respectively. The results for snapshots are shown in the top row. The results for the 4-day, 16-day and 31-day averages that are discussed in sections 6 and 7 are shown in the second, third and fourth rows, respectively. The resolution capabilities for divergence are much more sensitive to measurement noise, as evidenced by the steeper slopes of the lines in the left panels compared with the right panels that is evident visually even without taking into consideration the larger dynamic range of the ordinates of the left panels.

In the analysis that follows, the resolution capabilities of WaCM estimates of time-averaged divergence and vorticity are investigated from consideration of 4-day and 16-day averages of surface current measurements. In an effort to further reduce the measurement noise in estimates of divergence, averaging over 31 days is considered in section 7. Since the analysis here assumes a 4-day exact repeat satellite orbit, averages over 4 and 16 days correspond to one and four exact-repeat periods of the orbit. For the 98.7° orbit inclination and 1800-km swath width assumed here, ascending orbits are nearly aligned with the alongshore orientation of the model grid and measurements are obtained over two 850-km swaths separated by a 100-km nadir gap along the satellite ground track (see the left panel of Fig. 9). A single swath is thus wider than than the 600-km across-shore extent of the CCS model grid. With the ascending node of the simulated orbits used here, a small portion of the northwest corner of the model grid lies within the nadir gap on this particular orbit.

A detailed description of the space-time sampling pattern of the simulated WaCM data considered here is given in sections 7 and 10.2 of C19. For an 1800-km swath width, the numbers of samples during each 4-day repeat period range from 5 to 7 (see the top panel of Fig. 10). The numbers of samples during a 16-day period increase by a factor of four (see the bottom panel of Fig. 10). Since the averaging of N observations reduces the uncorrelated noise by a factor of $N^{-1/2}$, the measurement noise will be attenuated by more than a factor of 2 in 4-day averages and by about a factor of 5 in 16-day averages. Whether this noise suppression significantly improves the S/N ratio depends on how much the signal is attenuated in the time-averages, as well as on the magnitudes of the sampling errors that are introduced by the time averaging. Because of the broad coverage as summarized above, it can be anticipated that sampling errors over a domain the size of the CCS model used here to simulate WaCM data will generally be of secondary concern compared with measurement noise.

The data processing procedure followed here to simulate the space-time sampling of WaCM data is summarized in detail in section 8.2 of C19. In addition to temporal averaging, spatial smoothing was applied with half-power filter cutoff wavelengths ranging from 10 to 200 km. The results for the divergence fields constructed from spatially smoothed 4-day averages of simulated WaCM data are shown by the solid lines in the left panels of Fig. 11 for speed noise standard deviations of $\sigma_{spd} = 0.25$, 0.15 and 0.05 m s^{-1}. Because the analysis here is based on simulated data with

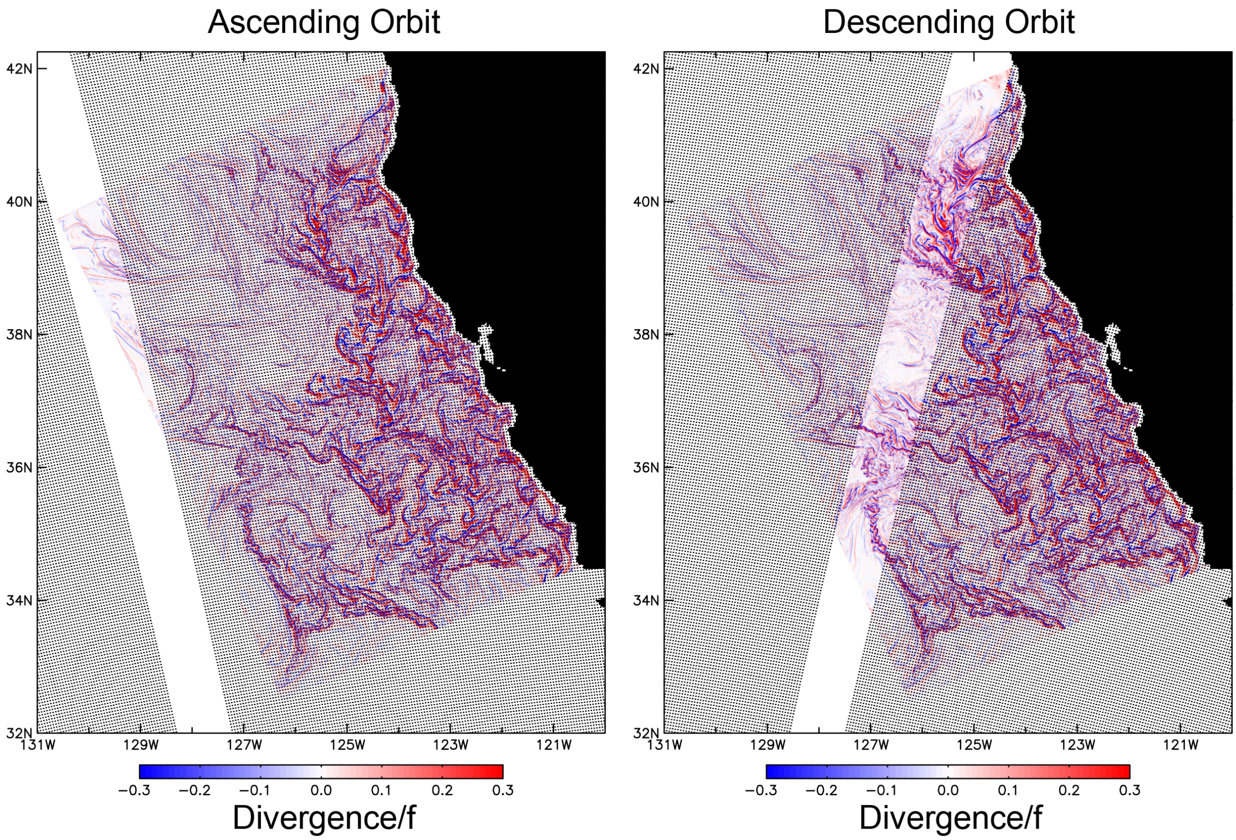

FIG. 9. Examples of the measurement swaths for single ascending and descending overpasses of WaCM for a swath width of 1800 km with a 100-km gap along the satellite ground track. The measurement swaths shown in gray are overlaid on the snapshot of δ/f shown in the top panel of Fig. 1c, except in non-rotated longitude-latitude coordinates. The simulations in this study have assumed the same orbit configuration as the QuikSCAT satellite, which was a retrograde orbit with an inclination of 98.7°, an altitude of 802.7 km and a 4-day exact repeat with 57 orbits per repeat period. The precise locations of the ground tracks could be adjusted to optimize the sampling of any specific region.

imposed measurement noise and sampling at the times and locations within specified measurement swaths, the effects of each source of error can be examined separately by computing the divergence and vorticity from complete model output over the averaging period and from the noisy simulated observations within only the simulated measurement swaths at the times of the overpasses of the satellite. The dotted lines in Fig. 11 are the S/N standard deviation ratios from the effects of uncorrelated measurement noise alone. The dashed lines are the S/N ratios from sampling errors

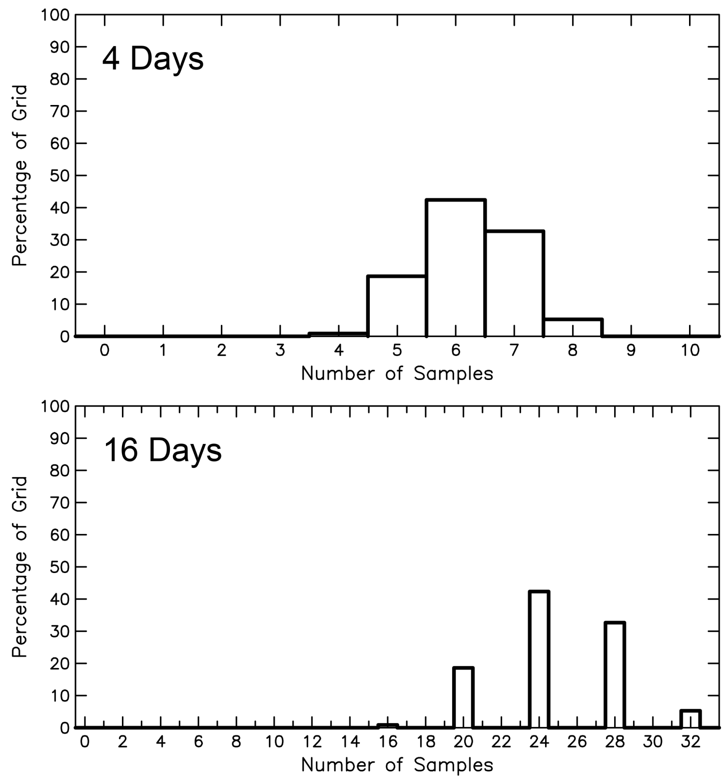

FIG. 10. Histograms of the numbers of samples by WaCM for a swath width of 1800 km with a 100-km gap along the satellite ground track during 4 days and 16 days of the orbit assumed here that has an exact repeat period of 4 days. The histogram values are expressed as percentages of the total number of grid points in the CCS model domain.

alone based on the simulated swath sampling of error-free fields. Note that the S/N ratios for the sampling errors are the same in all three panels in the left column of Fig. 11.

The very close agreement between the solid and dotted lines in Fig. 11 for the cases of speed noise standard deviations of $\sigma_{spd} = 0.25$ and 0.15 m s^{-1} indicates that the errors are almost totally dominated by measurement noise. If the measurements were error free, the resolution capability in 4-day averages of divergence for a threshold S/N standard deviation ratio of $\gamma = 3.16$ would be about 30 km, which is the wavelength at which the dashed lines have a S/N ratio of 3.16. For $\sigma_{spd} = 0.25$ m s^{-1} (the top left panel of Fig. 11), the resolution capabilities for estimates of 4-day averages of noisy divergence are coarser than the maximum value of 200 km on the abscissa, even for a liberal threshold criterion of $\gamma = 2.00$. For a smaller noise of $\sigma_{spd} = 0.15$ m s^{-1} (the middle

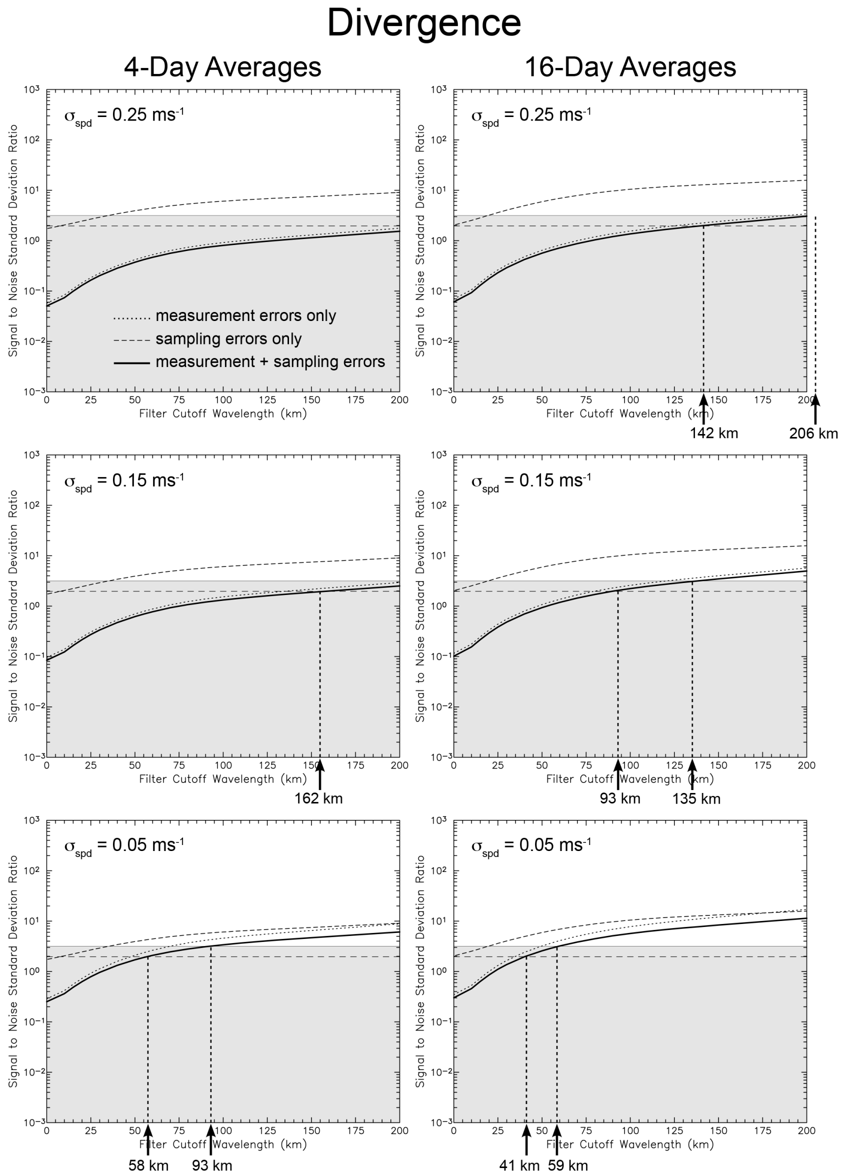

594 FIG. 11. The scale dependences of the S/N standard deviation ratios of smoothed signal and errors for the full CCS region for WaCM estimates of 4-day and 16-day averages of divergence after isotropic 2-dimensional smoothing using Parzen smoothers with the half-power filter cutoff wavelengths indicated along the abscissas for speed noise standard deviations of $\sigma_{spd} = 0.25$, 0.15 and 0.05 m s^{-1} (top to bottom). The three curves in each panel are the S/N ratios based on measurement noise alone (dotted lines), sampling errors alone (dashed lines) and combined measurement noise and sampling errors (solid lines). The gray areas, horizontal dashed line and vertical dashed lines are the same as in Fig. 5.

left panel of Fig. 11), the resolution capability is about 265 km for a threshold of $\gamma = 3.16$ (see Fig. 8) and 162 km for $\gamma = 2.00$.

In the highly optimistic scenario of a speed noise standard deviation of $\sigma_{spd} = 0.05$ m s^{-1}, the resolution capability in 4-day averages of divergence for a threshold criterion of $\gamma = 3.16$ improves to 93 km. It is evident from the spreading of the solid and dotted lines with increasing filter cutoff wavelength λ_c in the bottom left panel of Fig. 11 that the total errors are still dominated by measurement noise, but that the effects of measurement noise become decreasingly important with increasing filter cutoff wavelength λ_c.

The S/N ratios significantly improve in 16-day averages of divergence (the right panels of Fig. 11). By the threshold criterion of $\gamma = 3.16$, the resolution capabilities are 206, 135 and 59 km for speed noise standard deviations of $\sigma_{spd} = 0.25$, 0.15 and 0.05 m s^{-1}. An example 16-day average of divergence computed from simulated WaCM data with spatial smoothing of 135 km is shown in Fig. 12 for the case of a speed noise standard deviation of $\sigma_{spd} = 0.15$ m s^{-1}, which appears to be achievable in conditions of sufficiently high winds (see Fig. 2 of Wineteer et al. 2020).

Graphs of the S/N standard deviation ratio as functions of filter cutoff wavelength λ_c for 4-day and 16-day averages of WaCM estimates of vorticity are shown in Fig. 13 for the same cases of speed noise standard deviation $\sigma_{spd} = 0.25$, 0.15 and 0.05 m s^{-1} considered for divergence in Fig. 11. Because of the much stronger signal variance in vorticity, the resolution capabilities are dramatically better than for estimates of divergence. Examples of 4-day and 16-day averages of vorticity computed from simulated WaCM data spatially smoothed with filter cutoff wavelengths of $\lambda_c = 35$ and 25 km, respectively, are shown in Fig. 14 for the same speed noise standard deviation of $\sigma_{spd} = 0.15$ that was considered for Fig. 12. These are the approximate filter cutoff wavelengths that correspond to a S/N ratio of $\gamma = 3.16$. The small-scale features that are evident in these maps will yield new observational insight into the nature of variability on space and time scales in the transitional regime between mesoscale and submesoscale that cannot presently be addressed from any observational dataset.

The procedure used to generate the graphs in Figs. 11 and 13 was applied for speed noise standard deviations ranging from $\sigma_{spd} = 0.05$ to 0.50 m s^{-1}. The resolution capabilities are summarized graphically for 4-day and 16-day averages of divergence and vorticity in the second and third rows of Fig. 8 based on threshold S/N standard deviation ratios of $\gamma = 3.16$ and 2.00 (solid and dashed

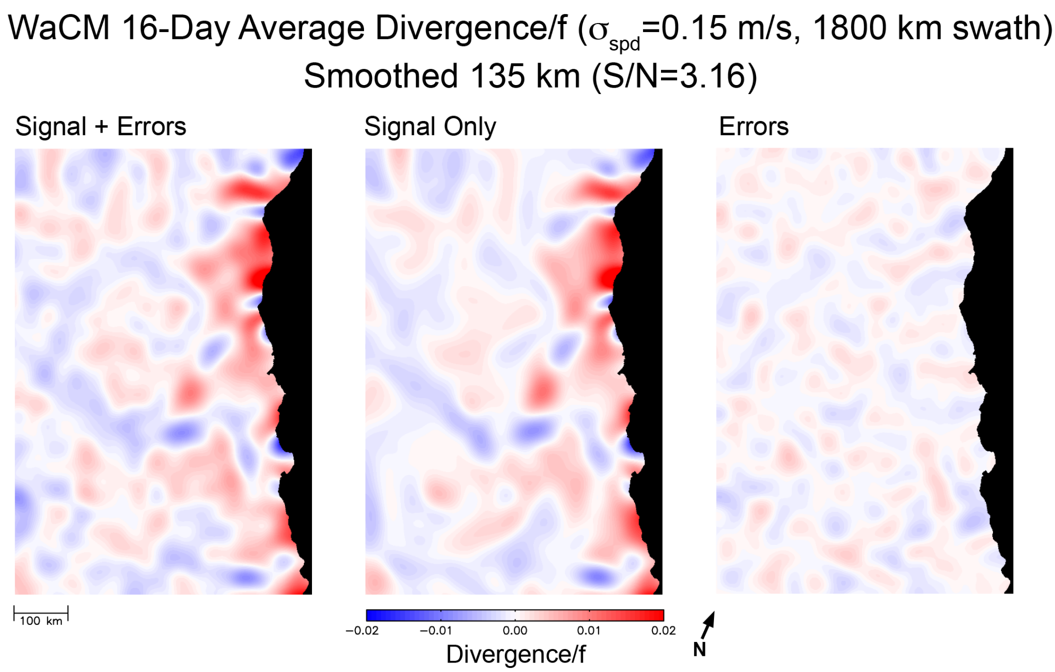

FIG. 12. Representative 16-day average maps of noisy (left panels) and error-free (middle panels) divergence and the associated errors (right panels) computed from simulated WaCM measurements of surface velocity with a speed noise standard deviation of $\sigma_{spd} = 0.15$ m s^{-1}. The signal and noise were smoothed using a Parzen smoother with a half-power filter cutoff wavelength of $\lambda_c = 135$, which corresponds to a S/N standard deviation ratio of $\gamma = 3.16$ (see the middle right panel of Fig. 11). For reference, a divergence of $\delta/f = 0.02$ at the central latitude 37°N of the model corresponds to a vertical velocity of about 0.76 m day^{-1} when integrated to a depth of 5 m.

lines, respectively). Compared with the graphs of the resolution capabilities for snapshots in the top panels, the improvements in the resolution capability in 4-day 16-day averages is more modest for divergence than for vorticity. This is because the divergence signals are more attenuated than the vorticity signals in the time averages. From the steeper slopes of the lines in all of the left panels of Fig. 8 compared with the right panels, it is apparent that estimates of divergence are much more sensitive to measurement noise than are estimates of vorticity.

7. The divergence associated with wind-driven coastal upwelling

In an effort to reduce the errors in simulated WaCM estimates of divergence beyond that which can be achieved with the 16-day averaging considered in section 6, the averaging time was increased

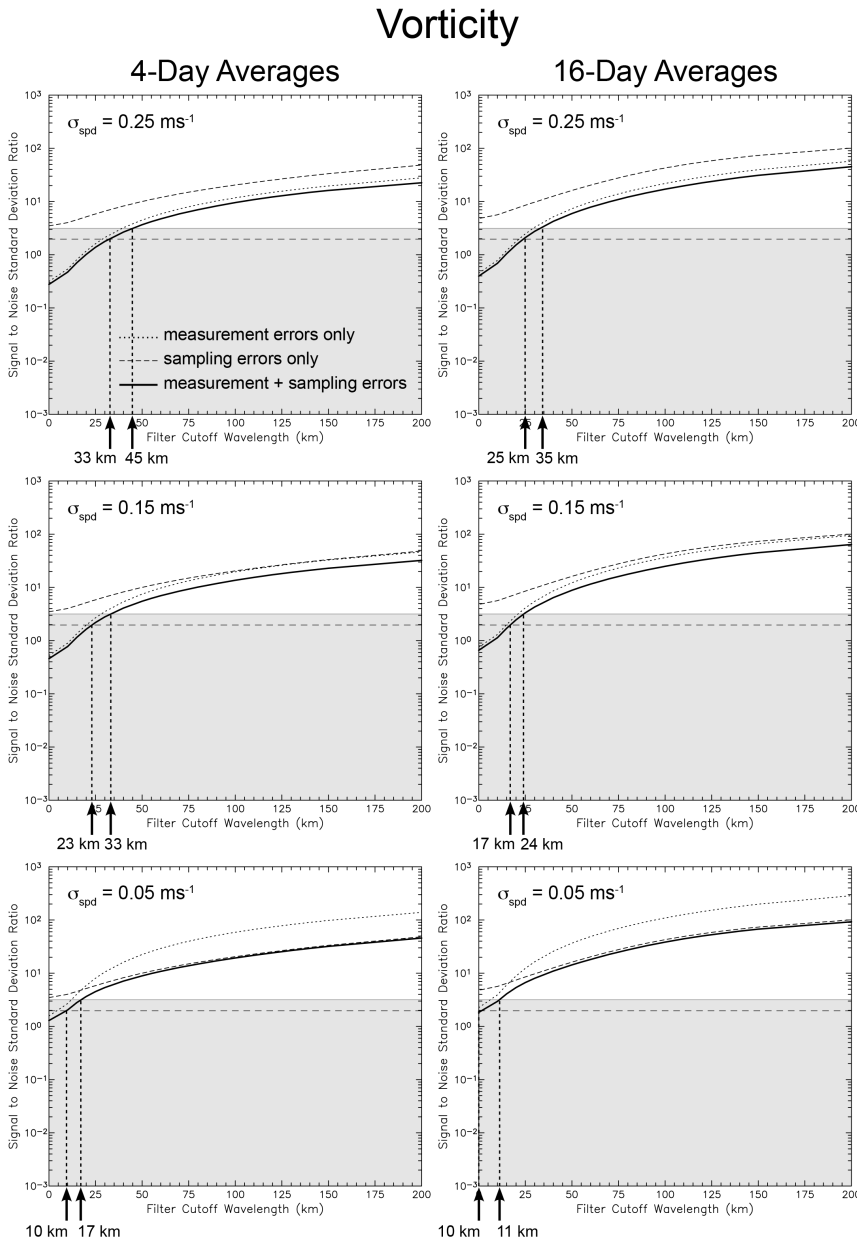

FIG. 13. The same as Fig. 11, except 4-day and 16-day averages of vorticity.

to 31 days. The scale dependence of the S/N standard deviation ratios computed over the full CCS model domain from a 31-day average of simulated WaCM data is shown in the left panels of Fig. 15 for speed noise standard deviations of $\sigma_{spd} = 0.25$, 0.15 and 0.05 m s^{-1}. The resolution capabilities for other choices of σ_{spd} are summarized graphically in the bottom left panel of Fig. 8. The increased resolution capabilities compared with the 16-day averages in the right panels of Fig. 11 and the third row of Fig. 8 are modest because the 31-day averages attenuate the divergence

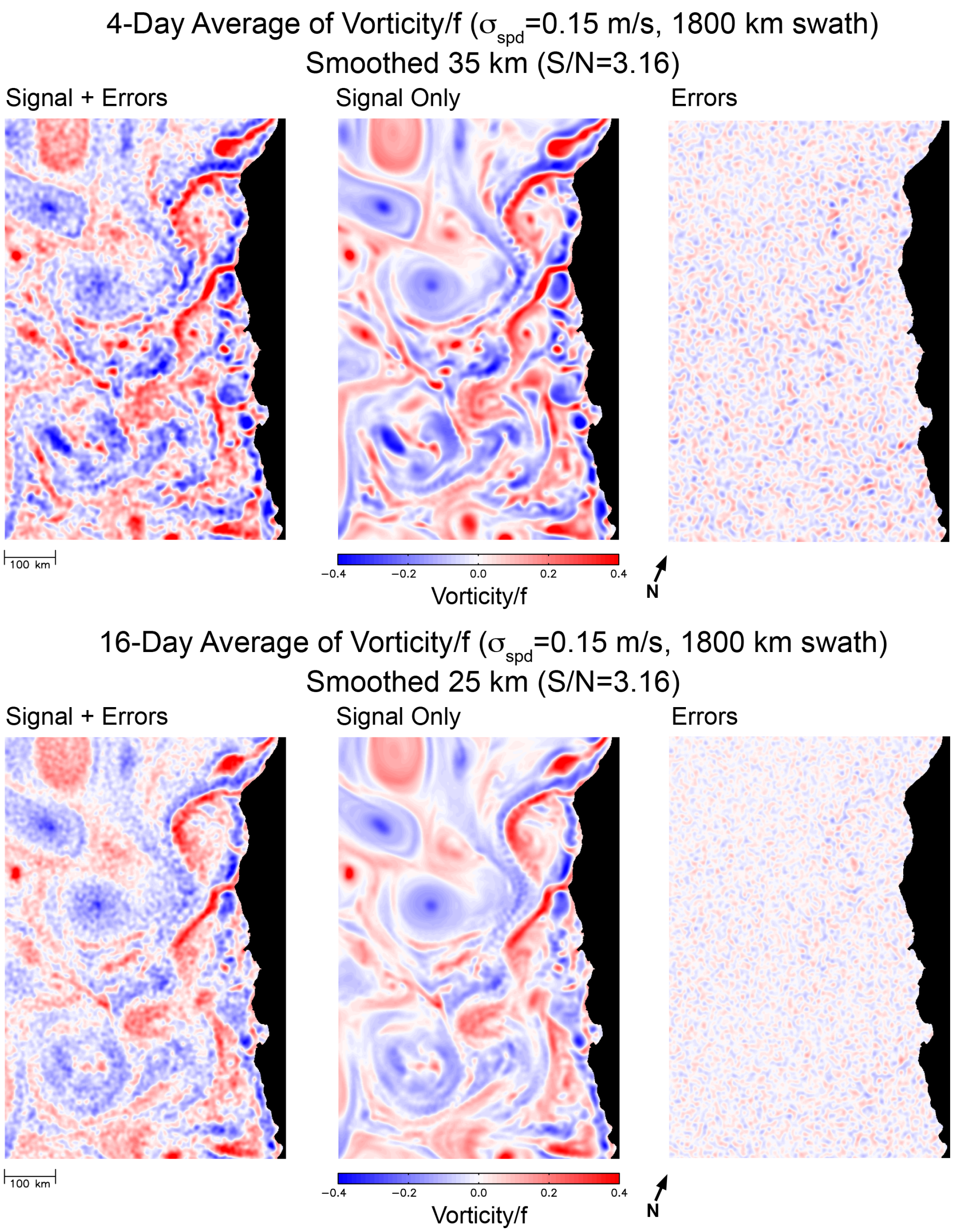

FIG. 14. Representative 4-day and 16-day average maps of noisy (left panels) and error-free (middle panels) vorticity and the associated errors (right panels) computed from simulated WaCM measurements of surface velocity with a speed noise standard deviation of $\sigma_{spd} = 0.15$ m s^{-1}. The signal and noise were smoothed using Parzen smoothers with half-power filter cutoff wavelengths of $\lambda_c = 35$ km (top) and 25 km (bottom), which correspond to S/N standard deviation ratios of approximately $\gamma = 3.16$ (see the middle panels of Fig. 13).

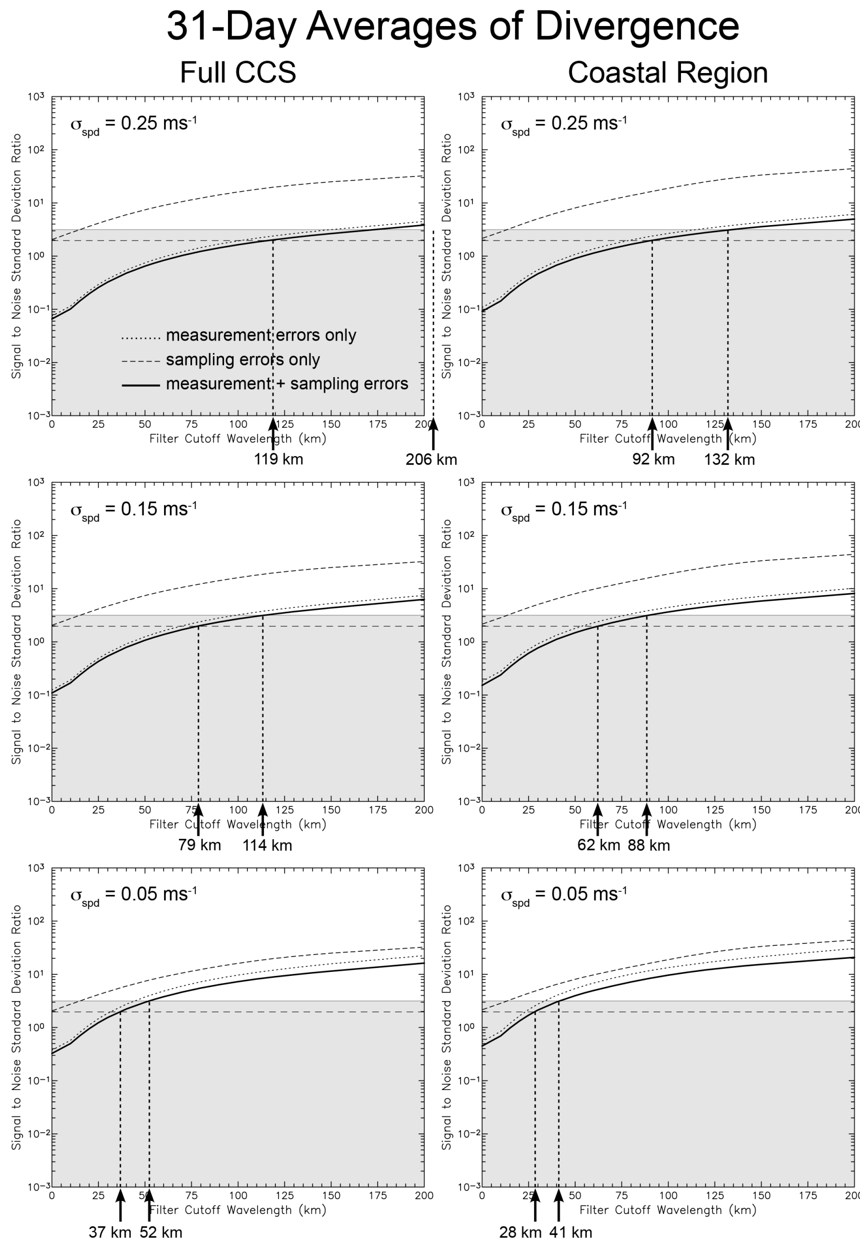

FIG. 15. The same as Fig. 11, except 31-day averages of divergence only. The left panels are the S/N standard deviation ratios computed over the full CCS model domain. The right panels are for the "coastal region" defined to be the region within about 150 km of the coast (see the boxes in the maps in Figs. 16 and 17).

signals nearly as much as the errors over most of the CCS domain. Estimation of divergence in the open ocean will thus be a challenge in the offshore region of the CCS. Within about 150 km of the coast, however, the divergence associated with wind-driven coastal upwelling is stronger and more persistent than it is farther offshore. If the divergence signals in this “coastal region" are not attenuated as much as the errors in the 31-day average, the S/N standard deviation ratio will increase, thus improving the resolution capability of WaCM estimates of divergence.

The S/N standard deviation ratios for divergence estimates computed from 31-day averages of simulated WaCM data in just the region within about 150 km of the coast (see the boxes in Fig. 16) are shown in the right panels of Fig. 15 for speed noise standard deviations of σ_{spd} = 0.25, 0.15 and 0.05 m s^{-1}. The improvements in the resolution capability compared with the assessments in the left column of Fig. 15 computed for the full CCS model domain are indeed significant.

Divergence estimates computed from a 31-day average of simulated WaCM data are shown in Fig. 16 for the full CCS model domain for the cases of speed noise standard deviations of σ_{spd} = 0.25 and 0.15 m s^{-1} with isotropic spatial smoothing with filter cutoffs of λ_c = 130 and 90 km, respectively, which correspond to a S/N ratio of approximately $\gamma = 3.16$ in the coastal region for each choice of σ_{spd}. The divergence estimates in the offshore region are quite noisy. Within the boxes, however, the strongest divergences are associated with topographic features along the coastline that are known areas of strong and often persistent coastal upwelling.

As noted previously, the smoothed estimates of divergence near the coast (within about 40 km for λ_c = 130 and about 25 km for λ_c = 90) must be interpreted with caution because of the potential for contamination by edge effects of the smoothing. For a more liberal choice than $\gamma = 3.16$ for the threshold criterion to define the resolution capability, the smoothing could be decreased, thus allowing uncorrupted smoothed estimates of divergence closer to the coast. For example, a criterion of $\gamma = 2.00$ (which is likely too liberal, as discussed previously from Figs. 6 and 7; see also Fig. 8 of C19), the required smoothing for noise standard deviations of σ_{spd} = 0.25 and 0.15 m s^{-1} is about λ_c = 90 and 60 km, respectively (see the upper right two panels of Fig. 15).

The best combination of time averaging and spatial smoothing depends on how much the signal is attenuated by each aspect of the smoothing. In regions where the divergence is strong but less persistent, it may be advantageous to reduce the averaging time at the expense of having to increase the spatial smoothing. The procedure followed to generate the S/N graphs in the right column of Fig. 15 were applied to the case of 16-day averages in just the region within about 150 km of the coast. The results (not shown here) conclude that the smoothing required to achieve a S/N ratio of $\gamma = 3.16$ is λ_c = 160 and 100 km for noise standard deviations of σ_{spd} = 0.25 and 0.15 m s^{-1},

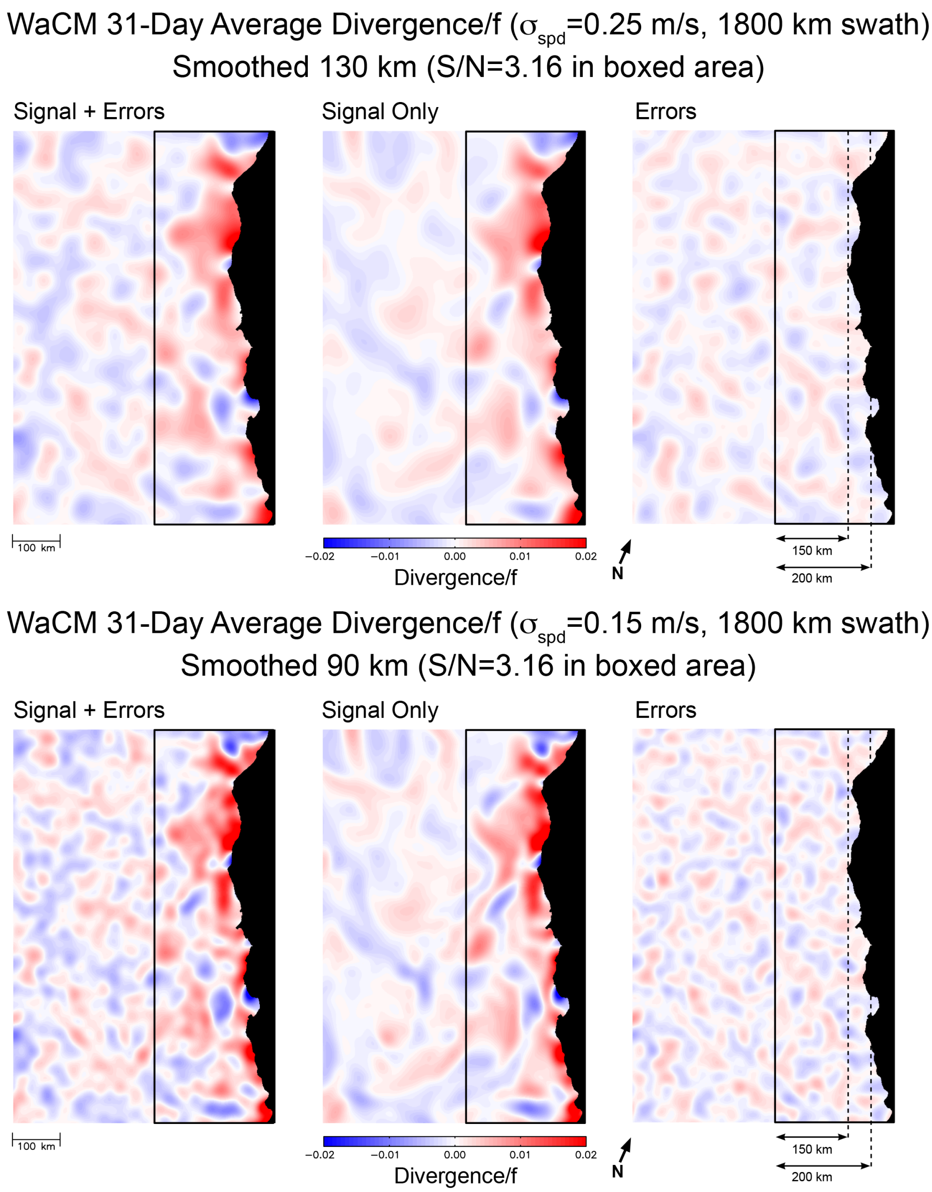

FIG. 16. Maps of noisy (left panels) and error-free (middle panels) vorticity and the associated errors (right panels) computed from simulated WaCM measurements of surface velocity averaged over 31 days with speed noise standard deviations of $\sigma_{spd} = 0.25$ and 0.15 m s^{-1} (top and bottom). The signal and noise were smoothed using Parzen smoothers with half-power filter cutoff wavelengths of λ_c = 130 km (top) and 90 km (bottom), which correspond to S/N standard deviation ratios of approximately γ = 3.16 within the box overlaid in each panel (see the top two right panels of Fig. 15). For reference, a divergence of $\delta/f = 0.02$ at the central latitude 37°N of the model corresponds to a vertical velocity of about 0.76 m day^{-1} when integrated to a depth of 5 m.

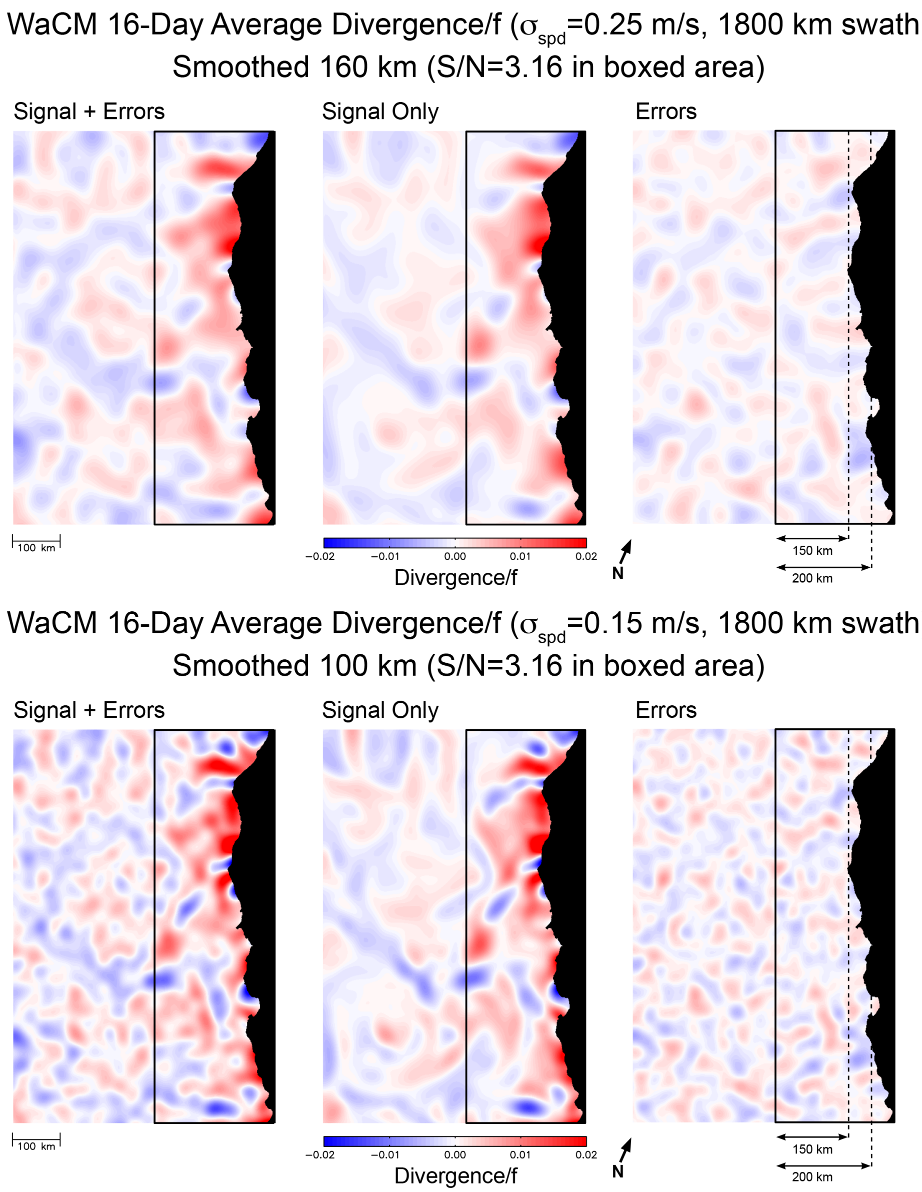

FIG. 17. The same as Fig. 16, except from simulated WaCM measurements of surface velocity averaged over 16 days with speed noise standard deviations of $\sigma_{spd} = 0.25$ and 0.15 m s^{-1} (top and bottom). The signal and noise were smoothed using Parzen smoothers with half-power filter cutoff wavelengths of $\lambda_c = 160$ km (top) and 100 km (bottom), which correspond to S/N standard deviation ratios of approximately $\gamma = 3.16$ (not shown here) within the box overlaid in each panel. For reference, a divergence of $\delta/f = 0.02$ at the central latitude 37°N of the model corresponds to a vertical velocity of about 0.76 m day^{-1} when integrated to a depth of 5 m.

respectively. The latter is significantly smaller than the value of $\lambda_c = 135$ km that was required for $\gamma = 3.16$ over the full CCS domain for $\sigma_{spd} = 0.15$ m s^{-1} (see Figs. 11 and 12).

Maps of 16-day averages of divergence for $\gamma = 3.16$ within the coastal region are shown in Fig. 17 for $\sigma_{spd} = 0.25$ and 0.15 m s^{-1} and the above filter cutoff wavelengths of $\lambda_c = 160$ and 100 km. The divergence fields within the boxes in Fig. 17 are similar to those in Fig. 16 for 31-day averages, but with visually more energetic small-scale structures despite the somewhat larger spatial smoothing in Fig. 17. This seeming inconsistency is because of the greater attenuation and smoothing of the temporally evolving divergence signal in 31-day averages than in 16-day averages. As a consequence, more variability of divergence is retained at small scales in 16-day averages, even with the somewhat higher spatial smoothing required to achieve the S/N ratio of $\gamma = 3.16$.

8. Summary and Conclusions

The analysis procedures developed and applied by Chelton et al. (2019; referred to here as C19) to estimates of surface ocean velocity and vorticity from a future satellite Doppler scatterometer Winds and Currents Mission (WaCM) were applied in this study to assess the resolution capabilities of WaCM estimates of divergence. In light of recent results by Wineteer et al. (2020) that conclude that satellite Doppler measurements of surface ocean velocity can be obtained with higher accuracies than were considered feasible by C19, the present study also revisits the assessment of resolution capability of WaCM estimates of vorticity. Because divergence is much less energetic than vorticity and is more restricted to small spatial scales (Figs. 1 and 2), the resolution capability for WaCM estimates of divergence is much coarser than for vorticity. Moreover, estimates of divergence are much more sensitive to measurement noise than are estimates of vorticity (see Fig. 8). Useful estimates of divergence will likely only be possible with measurement accuracies that push the limits of present technology.

When possible, the example maps presented here (Figs. 7, 12, 14 and the bottom panels of Figs. 16 and 17) focused on measurements with speed noise standard deviations of $\sigma_{spd} = 0.15$ m s^{-1}, which appears to be feasible (and generally necessary in the case of divergence) over much of the measurement swaths for winds stronger than about 6 m s^{-1} (see Fig. 2 of Wineteer et al. 2020), which is somewhat lower than the global average wind speed of 7.4 m s^{-1} (Wentz et al. 1986). A highly optimistic speed noise standard deviation of $\sigma_{spd} = 0.05$ m s^{-1} is required to achieve the desired S/N ratio for snapshots of divergence (Figs. 5 and 6).

The analysis here considered only the non-internal-wave contributions to surface current divergence and vorticity, which are likely of greater interest than the interrnal-wave contributions to most researchers. This is achieved by simulating noisy WaCM measurements of surface ocean velocity using the ROMS model of the California Current System (CCS) summarized in section 2 that has high dissipation, was forced only by seasonal cycles of wind stress and heat and freshwater fluxes, and does not include tidal forcing. Internal wave signals are therefore weak in the model. While this is a misrepresentation of the real ocean, it is advantageous for the purposes of this study. The model used by Wineteer et al. (2020) is likely a better representation of reality, but is dominated by internal wave signals on small scales in the divergence field, and to a lesser extent the vorticity field. The question of how the internal-wave contributions to divergence can be mitigated in actual future WaCM data is not addressed in this study. It is hoped that the time averages that will be required to achieve adequate S/N ratio in estimates of divergence (Fig. 8) will also sufficiently suppress internal wave signals.

It is noteworthy that the surface ocean velocity in the simulated WaCM data derived from the model summarized in section 2 has been defined here to be the upper-level velocity of the model. The thickness of the upper level of the terrain-following vertical grid of the ROMS model is about an order of magnitude smaller over the continental shelf than in the deep ocean. This geographical variation of upper-level thickness is a potentially important concern that has not yet been addressed in the simulation of WaCM measurements of surface ocean velocity.

To simulate sampling by a future WaCM, it was assumed that the satellite will have the same orbit as QuikSCAT, which consists of an inclination of 98.7° and an exact repeat period of 4 days. It has also been assumed that the measurement swath will consist of an 1800-km swath with a 100-km gap centered on the satellite ground track, and that the WaCM measurements will be smoothed in onboard pre-processing to have a footprint diameter of 5 km. The measurement noise has been assumed to be spatially homogeneous across each of the two parallel 850-km swaths and equally partitioned between the two orthogonal velocity components. In reality, the noise of each component will vary across the measurement swaths in a manner that results in increasing noise in the along-track component toward the outer edges of the swaths and increasing noise in the across-track component toward the inner edges of the swaths (see Fig. 13 of Rodríguez 2018). The analysis presented here may therefore be optimistic, especially near the edges of the measurement swaths. The wind speed dependence of the measurement noise reported by Wineteer et al. (2020) was also not considered in this study.

It should be noted that Eqs. (A2), (A5), (B1), (B3), (B4) and (B5) that are presented in the appendices for the residual noise variance and wavenumber spectral characteristics of divergence and vorticity computed from noisy WaCM measurements of u and v are expressed in terms of the individual noise standard deviations σ_u and σ_v of each velocity component. Those expressions are therefore applicable to any specified measurement noise standard deviation at any location within the measurement swaths and for any ambient wind conditions. With the assumptions here that the measurement noise is equally partitioned between u and v, the standard deviations of the velocity components can be written as $\sigma_u = \sigma_v \equiv \sigma_{u,v} = 2^{-1/2}\sigma_{spd}$. The noise is then fully characterized by specification of the speed measurement noise σ_{spd}.

The resolution capability for non-internal-wave contributions to divergence and vorticity is assessed here from the ratio of the standard deviations of the error-free signals computed from the CCS model output and the errors in the estimates constructed from simulated noisy WaCM data obtained from space-time sampling of the model output at the times and locations of the satellite overpasses. These signal and noise standard deviations were both computed over the region of interest with the same spatial smoothing and temporal averaging. For the analysis presented in sections 5 and 6, the region of interest was the full CCS model domain, except that the areas within 50 km of the northern, western and southern boundaries were excluded to mitigate edge effects from spatial smoothing. In section 7, a smaller “coastal region" was considered within about 150 km of the California coastline

For the instantaneous snapshots considered in section 5, the errors consist almost exclusively of the effects of measurement noise on the estimates of divergence and vorticity. The only sampling errors in snapshots are artifacts from edge effects of spatial smoothing that can arise near swath edges and coastal boundaries.

In the 4-day, 16-day and 31-day averages considered in sections 6 and 7, the errors consist of measurement noise plus sampling errors that can arise from rapidly evolving submesoscale variability that is not adequately resolved by the space-time sampling of the surface velocity field within the simulated WaCM measurement swaths. For estimation of divergence, it was shown that sampling errors are negligible compared with measurement errors unless the measurement noise is less than 0.05 m s^{-1}, in which case measurement errors decrease in importance with increased spatial smoothing (Fig. 11). Measurement errors are somewhat less of an issue for estimation of vorticity (Fig. 13). Because the satellite sampling will not resolve the time-evolution of rapidly evolving internal waves, and these waves are underrepresented in the model used to simulate WaCM data in this study, sampling errors will be a more significant concern in actual WaCM data than has been inferred here. The effects of these sampling errors can be investigated by simulating WaCM data constructed from a model such as that used by Wineteer et al. (2020) that has a more realistic representation of internal waves. Efforts are presently underway to assess the effectiveness of time averaging to suppress internal wave signals in simulated Doppler scatterometer data from that model.

Time averaging and spatial smoothing to attenuate the effects of measurement noise and sampling errors also attenuates the signals of interest. However, the errors are generally attenuated more than the signals. The S/N ratio therefore increases with increased temporal averaging and spatial smoothing (Figs. 5, 11, 13 and 15). Defining the resolution capability requires a subjective specification of a threshold minimum S/N standard deviation ratio. The choice of $\gamma = 3.16$ (which corresponds to a S/N variance ratio of 10) that was advocated by C19 has been adopted here based on visual comparisons of noisy and error-free fields with various values of γ (see, for example, Figs. 6 and 7). The resulting resolution capabilities are summarized graphically by the solid lines in Fig. 8 as functions of the speed measurement noise σ_{spd} for snapshots and averages over 4, 16 and 31 days. For readers who feel that a threshold criterion lower than $\gamma = 3.16$ is justified, the resolution capabilities for a choice of $\gamma = 2.00$ that corresponds to a S/N variance ratio of 4 (which is likely too liberal) are summarized graphically by the dashed lines in Fig. 8. Thresholds of $\gamma = 3.16$ and 2.00 correspond to correlations of 0.95 and 0.89, respectively, between the smoothed error-free field and the smoothed field constructed from simulated observations with measurement noise and sampling errors (see section 5 of C19).

Regardless of the choice of threshold criterion for γ shown in Fig. 8, it is readily apparent that estimation of non-internal-wave contributions to divergence is much more challenging than estimation of vorticity. For snapshots and 4-day averages, wavelength resolutions better than 250 km for divergence can only be achieved with very small measurement noise. Averaging over 16 or 31 days can improve those resolution capabilities to 100–150 km, depending on how small a value of the speed measurement noise standard deviation σ_{spd} can be achieved. Low measurement noise will be most feasible near the centers of the measurement swaths in moderate to high wind speed conditions (see Fig. 2 of Wineteer et al. 2020). As summarized graphically in the right column of Fig. 8, much higher resolutions will be possible for WaCM estimates of vorticity. Representative maps of divergence and vorticity fields with S/N ratios of $\gamma = 3.16$ are shown in Figs. 6, 7, 12, 14, 16 and 17.

The conclusions from this study are based on simulated WaCM data from the specific model of summertime conditions in the CCS region summarized in section 2. The resolution capabilities in other regions of the ocean where the divergence and vorticity signals are stronger will be better than suggested from Fig. 8. For example, the non-internal-wave contributions to the divergence field in the model considered here are more energetic in the region within about 150 km of the coast than farther offshore. The resolution capability is therefore better in the coastal region. Even higher resolutions may be possible in regions such as the Gulf Stream where non-internal-wave contributions to small-scale signals in divergence and vorticity may be more energetic than in the CCS region (Wineteer et al. 2020).

Acknowledgments. This research was supported by NASA Grants 80NSSC19K0061 and 80NSSC19K1011. I thank Michael Schlax for development of many of the computer codes that were adapted herein for application to divergence fields computed from simulated satellite Doppler scatterometer measurements of surface currents. Roger Samelson's insightful discussions throughout the course of this study and his thorough and detailed comments on the manuscript are greatly appreciated. I also thank Melanie Fewings for suggesting the analysis in section 7.

Data availability statement. The ocean surface velocity fields from the model of the California Current System that were used to simulate satellite Doppler scatterometer measurements of surface currents in this study were obtained from Jeroen Molemaker at the University of California at Los Angeles.

APPENDIX A

The standard deviations of divergence and vorticity noise

The effects of uncorrelated measurement errors in the across-shore velocity component u and alongshore velocity component v on estimates of vorticity $\zeta = \partial v/\partial x - \partial u/\partial y$ obtained using 3-point centered difference approximations of the derivatives are derived by propagation-of-error analysis in appendix G.2 of C19. The general expression for the variance of the vorticity errors is Eq. (G.14), which is

$$\sigma_\zeta^2 = \frac{\sigma_v^2}{2\Delta x^2}\left[1-\rho_v(2\Delta x)\right] + \frac{\sigma_u^2}{2\Delta y^2}\left[1-\rho_u(2\Delta y)\right], \tag{A1}$$

where Δx and Δy are the grid spacings in the across-shore x and alongshore y dimensions, and $\rho_v(2\Delta x)$ and $\rho_u(2\Delta y)$ are the autocorrelations of, respectively, the errors of the alongshore velocity component at a spatial lag of $2\Delta x$ and the across-shore velocity component at a spatial lag of $2\Delta y$. Analogous to the derivation of (A1), it can be shown straightforwardly that the variance of the errors of divergence $\delta = \partial u/\partial x + \partial v/\partial y$ obtained using 3-point centered difference approximations of the derivatives has the same form as (A1), except that Δx and Δy are interchanged. For the case of equal grid spacing in each dimension and spatially homogeneous errors that is assumed here, $\Delta x = \Delta y \equiv \Delta$ and the lagged autocorrelations $\rho_u(2\Delta)$ and $\rho_v(2\Delta)$ of the errors are the same, which will be denoted as $\rho_{u,v}(2\Delta)$. The variance of the errors then becomes the same for both divergence and vorticity and reduces to

$$\sigma_{\zeta,\delta}^2 = \frac{\sigma_u^2+\sigma_v^2}{2\Delta^2}\left[1-\rho_{u,v}(2\Delta)\right]. \tag{A2}$$

The velocity component noise for a footprint diameter of 5 km is uncorrelated on a sample grid of 5 km × 5 km (see appendix B of C19). For the case of equal partitioning (1) of the measurement errors between u and v that is assumed in this study, $\sigma_u^2 = \sigma_v^2 \equiv \sigma_{u,v}^2 = \sigma_{spd}^2/2$ and the standard deviations of divergence and vorticity noise obtained from the square root of (A2) with $\rho_{u,v}(2\Delta) = 0$ simplify to

$$\sigma_{\zeta,\delta}\Big|_{5\text{km}} = \frac{1}{\Delta}\sigma_{u,v} = \frac{1}{\sqrt{2}\Delta}\sigma_{spd}, \tag{A3}$$

where $\Delta = 5$ km is the grid spacing in both the x and y dimensions. For the case of $\sigma_{spd} = 0.25$ m s^{-1}, for example, this is

$$\sigma_{\zeta,\delta}\Big|_{5\text{km}} = 3.54\times10^{-5}\,\text{s}^{-1} = 0.40 f_{37^\circ\text{N}}, \tag{A4}$$

where $f_{37^\circ\mathrm{N}} = 8.8 \times 10^{-5}$ s^{-1} is the Coriolis parameter at the central latitude 37°N of the CCS model domain.

It is shown in appendix H of C19 that it is advantageous to oversample the WaCM data with a grid spacing of $\Delta = 1$ km because the wavenumber filter response function of the centered difference approximation of the derivatives [see (B2) below] on the finer grid retains more of the high-wavenumber variability in the divergence and vorticity signals. This becomes more and more advantageous with increasing measurement accuracy (decreasing noise standard deviations σ_u and σ_v), which allows resolution of smaller and smaller spatial scales of divergence and vorticity variability. The footprint diameter of the measurements is still 5 km and the standard deviations of the errors of u and v are still σ_u and σ_v. However, the velocity component errors on the finer grid spacing of $\Delta = 1$ km are spatially correlated. For the Parzen smoother used here to simulate onboard pre-processing of the data to achieve a footprint diameter of 5 km on an oversampled 1-km grid by smoothing the raw data with a half-power filter cutoff wavelength of 10 km, it is shown in Fig. B.1b of C19 that the autocorrelation of the errors of u and v at a lag of $2\Delta = 2$ km is $\rho_{u,v}(2\Delta) = 0.638$. The variance (A2) of the divergence and vorticity noise on the oversampled 1-km grid with arbitrarily specified velocity component noise variances σ_u^2 and σ_v^2 then becomes

$$\sigma^2_{\zeta,\delta}\big|_{1\mathrm{km}} = \frac{0.362}{2\Delta^2}\left(\sigma_u^2 + \sigma_v^2\right). \tag{A5}$$

The expressions (A2) and (A5) for the variances of the divergence and vorticity noise are applicable to the realistic case of WaCM data with σ_u and σ_v that differ from each other, vary across the measurement swaths, and depend on the wind speed. For the simplified assumption in this study of equal partitioning of the measurement errors between u and v for a 5-km footprint diameter, the standard deviation of the divergence and vorticity noise on an oversampled 1 km × 1 km grid obtained from the square root of (A5) is

$$\sigma_{\zeta,\delta}\big|_{1\mathrm{km}} = \frac{\sqrt{0.362}}{\Delta}\sigma_{u,v} = \frac{\sqrt{0.181}}{\Delta}\sigma_{spd}, \tag{A6}$$

where $\Delta = 1$ km. For the case of $\sigma_{spd} = 0.25$ m s^{-1} considered in (A4), this is

$$\sigma_{\zeta,\delta}\big|_{1\mathrm{km}} = 10.6 \times 10^{-5}\,\mathrm{s}^{-1} = 1.2 f_{37^\circ\mathrm{N}}. \tag{A7}$$

Because of smaller grid spacing Δ, but the same standard deviation σ_{spd} of the measurement noise, the standard deviation of ζ and δ noise as expressed by (A6) and (A7) for the oversampled 1-km grid is 3 times larger than the standard deviation of the noise as expressed by (A3) and (A4) for the 5-km grid. The reason the ζ and δ noise standard deviations on the finer grid are not proportionally larger by the factor-of-5 difference in grid spacing Δ is that the amplification from the smaller value of Δ in the denominator of (A6) is mitigated by the nonzero autocorrelation at lag 2Δ in (A2) on the oversampled grid.

Vorticity and divergence fields with the noise standard deviation (A7) that is larger than the Coriolis parameter are not likely to be of much value scientifically. In accord with (A6), the noise standard deviation $\sigma_{\zeta,\delta}$ decreases proportionally with the standard deviation σ_{spd} of the measurement errors. But even for a highly optimistic case of a speed measurement noise standard deviation of only $\sigma_{spd} = 0.05$ m s^{-1}, the corresponding ζ and δ noise standard deviation (A6) is $\sigma_{\zeta,\delta} = 0.24 f_{37°\mathrm{N}}$. This is probably still too large for most applications, especially for divergence which has a more limited dynamic range than vorticity (see Fig. 2). It will therefore be necessary to reduce the noise in ground-based post-processing by spatially smoothing the noisy measurements of u and v. The reductions of the noise standard deviations in estimates of divergence and vorticity that are achieved by spatial smoothing are discussed in section 3 and shown graphically in Fig. 3.

APPENDIX B

The wavenumber spectral characteristics of divergence and vorticity noise

The scale dependence of the noise in vorticity estimated from 3-point centered differences of measurements of the velocity components with a footprint diameter of 5 km can be characterized by the alongshore wavenumber spectrum of the vorticity noise that is derived in appendix I.3 of C19. The result is Eq. (I.43) in C19, which is

$$\tilde{S}_{\zeta}(l) = \tilde{S}_{\partial u/\partial y}(l) + \tilde{S}_{\partial v/\partial x}(l), \tag{B1a}$$

where l is the alongshore wavenumber. The two terms on the right side of (B1a) can be expressed in terms of the standard deviations of the velocity component errors as Eqs. (I.45b) and (I.46a) of

C19, which are

$$\tilde{S}_{\partial u/\partial y}(l) = 10\,\Delta y\,\sigma_u^2 \left|W_{3pt}(l)\right|^2 W_{10\mathrm{km}}^2(l) \tag{B1b}$$

$$\tilde{S}_{\partial v/\partial x}(l) = 100\,\Delta x\,\Delta y\,\sigma_v^2\, W_{10\mathrm{km}}^2(l) \int_0^{k_N} \left|W_{3pt}(k)\right|^2 W_{10\mathrm{km}}^2(k)\,dk, \tag{B1c}$$

where $k_{\mathcal{N}} = (2\Delta x)^{-1}$ is the Nyquist wavenumber for a sample interval of Δx in the across-shore x dimension. The tildes in (B1a)–(B1c) are reminders that the raw WaCM data have been smoothed isotropically with a half-power filter cutoff wavelength of 10 km to achieve a footprint diameter of 5 km. The factors $W_{10\mathrm{km}}(l)$ and $W_{10\mathrm{km}}(k)$ are the filter transfer functions of the smoother in the alongshore and across-shore dimensions, respectively, for the half-power filter cutoff wavelength of 10 km, and

$$W_{3pt}(l) = i\,\frac{\sin(2\pi\Delta y\,l)}{\Delta y} \quad \text{and} \quad W_{3pt}(k) = i\,\frac{\sin(2\pi\Delta x\,k)}{\Delta x}. \tag{B2}$$

are the wavenumber response functions for 3-point centered difference approximations of the alongshore and across-shore derivatives, respectively, for grid spacings of Δy and Δx. The significance of the factor $i = \sqrt{-1}$ in the two expressions (B2) is that 3-point centered differencing introduces a quadrature phase shift at each wavenumber.

The integral on the right side of (B1c) depends on the particular choice of smoothing and must be evaluated numerically. The solution for the case of the Parzen smoother used here is shown graphically in Fig. I.1a of C19. For $\Delta x = 1$ km, the integral has a value of 0.0221 km^{-3}.

It is noteworthy that the derivations of (B1a)–(B1c) are based on separate 1-dimensional smoothing of the raw data with a half-power filter cutoff wavelength of 10 km in each dimension to simulate the pre-processing of WaCM data for a footprint diameter of 5 km. For the case of the Parzen smoother used here, it is shown in appendix C of C19 that this is essentially equivalent to isotropic smoothing with a 2-dimensional Parzen weighting function that depends only on the radial distance from the estimation location. Derivations of analytical expressions for the effects in the wavenumber domain of isotropic 2-dimensional smoothing are much simpler when the filter transfer function of the 2-dimensional smoother can be separated as the product of 1-dimensional filter transfer functions in each dimension.

The alongshore wavenumber spectrum of the noise in estimates of divergence can be derived analogous to the derivation in C19 of (B1a)–(B1c) above, resulting in

$$\tilde{S}_{\delta}(l) = \tilde{S}_{\partial u/\partial x}(l) + \tilde{S}_{\partial v/\partial y}(l), \tag{B3a}$$

where

$$\tilde{S}_{\partial u/\partial x}(l) = 100\,\Delta x\,\Delta y\,\sigma_u^2\,W_{10\mathrm{km}}^2(l)\int_0^{k_N}\left|W_{3pt}(k)\right|^2 W_{10\mathrm{km}}^2(k)\,dk \tag{B3b}$$

$$\tilde{S}_{\partial v/\partial y}(l) = 10\,\Delta x\,\sigma_v^2\left|W_{3pt}(l)\right|^2 W_{10\mathrm{km}}^2(l). \tag{B3c}$$

The expressions (B1) and (B3) are valid for arbitrary grid spacings Δx and Δy and arbitrary noise variances σ_u^2 and σ_v^2. For uniform grid spacing $\Delta x = \Delta y \equiv \Delta$ and equal partitioning of WaCM measurement errors between the u and v components so that $\sigma_u^2 = \sigma_v^2 \equiv \sigma_{u,v}^2 = \sigma_{spd}^2/2$, the sums on the right sides of (B1a) and (B3a) are exactly the same. The alongshore spectra of the divergence and vorticity noise are then the same. The resulting analytical expression is shown by the green lines in the top panels of Fig. 4 for measurement noise with speed standard deviations of $\sigma_{spd} = 0.50$, 0.25 and 0.10 m s^{-1}.

Derivation of analytical expressions for the alongshore wavenumber spectra of the residual noise in smoothed divergence and vorticity fields estimated from smoothed velocity component errors proceeds similarly to the analysis summarized above. The spectrum of smoothed vorticity noise is derived in appendix I.4 of C19, resulting in Eq. (I.52), which is

$$\overline{\tilde{S}}_{\zeta}(l) = \overline{\tilde{S}}_{\partial u/\partial y}(l) + \overline{\tilde{S}}_{\partial v/\partial x}(l), \tag{B4a}$$

where the two terms on the right side of (B4a) can be expressed as Eqs. (I.54a) and (I.55a) of C19, which are

$$\overline{\tilde{S}}_{\partial u/\partial y}(l) = 100\,\Delta x\,\Delta y\,\sigma_u^2\left|W_{3pt}(l)\right|^2 W_{10\mathrm{km}}^2(l)\,W_{\lambda_c}^2(l)\int_0^{k_N} W_{10\mathrm{km}}^2(k)\,W_{\lambda_c}^2(k)\,dk \tag{B4b}$$

$$\overline{\tilde{S}}_{\partial v/\partial x}(l) = 100\,\Delta x\,\Delta y\,\sigma_v^2\,W_{10\mathrm{km}}^2(l)\,W_{\lambda_c}^2(l)\int_0^{k_N}\left|W_{3pt}(k)\right|^2 W_{10\mathrm{km}}^2(k)\,W_{\lambda_c}^2(k)\,dk, \tag{B4c}$$

where $W_{\lambda_c}(l)$ and $W_{\lambda_c}(k)$ are the filter transfer functions of the smoother in the alongshore and across-shore dimensions, respectively, for the half-power filter cutoff wavelength of λ_c. The combined tildes and overbars in (B3a)–(B3c) signify that the spectra are computed from doubly smoothed measurement errors. The raw data are first smoothed with a half-power filter cutoff wavelength of 10 km in the simulated pre-processing of the raw data to obtain simulated measurements with a footprint diameter of 5 km. The resulting pre-processed data are then smoothed with a half-power filter cutoff wavelength of λ_c in simulated post-processing.

The integrals on the right side of (B4b) and (B4c) depend again on the particular choice of smoothing and must be evaluated numerically. The solutions for the case of the Parzen smoother used here are shown graphically in Figs. I.1c and I.1d of C19.

Equations (B4a)–(B4c) quantify the effects in the wavenumber domain of the double 2-dimensional smoothing of the noise in the estimates of vorticity. The derivation of the analytical forms (B4a)–(B4c) of this smoothing assumes that the filter transfer function of each 2-dimensional smoother can be separated as the product of 1-dimensional filter transfer functions in each dimension. As noted previously in the discussion of (B1a)–(B1c), the Parzen smoother used here for both the pre-processing and the post-processing is separable in this manner (see appendix C of C19).

The alongshore wavenumber spectrum of the residual noise in smoothed estimates of divergence can be derived analogous to the derivation in C19 of (B4a)–(B4c), resulting in

$$\overline{\tilde{S}}_{\delta}(l) = \overline{\tilde{S}}_{\partial u/\partial x}(l) + \overline{\tilde{S}}_{\partial v/\partial y}(l), \tag{B5a}$$

where

$$\overline{\tilde{S}}_{\partial u/\partial x}(l) = 100\,\Delta x\,\Delta y\,\sigma_u^2\,W_{10\mathrm{km}}^2(l)\,W_{\lambda_c}^2(l)\int_0^{k_N}\left|W_{3pt}(k)\right|^2 W_{10\mathrm{km}}^2(k)\,W_{\lambda_c}^2(k)\,dk \tag{B5b}$$

$$\overline{\tilde{S}}_{\partial v/\partial y}(l) = 100\,\Delta x\,\Delta y\,\sigma_v^2\,\left|W_{3pt}(l)\right|^2\,W_{10\mathrm{km}}^2(l)\,W_{\lambda_c}^2(l)\int_0^{k_N} W_{10\mathrm{km}}^2(k)\,W_{\lambda_c}^2(k)\,dk. \tag{B5c}$$

As in the previous equations (B1) and (B3) for the spectra of divergence and vorticity noise computed from the noise in pre-processed WaCM data, the expressions (B4) and (B5) for the spectra of smoothed vorticity and divergence noise are valid for arbitrary grid spacings Δx and Δy and arbitrary noise variances σ_u^2 and σ_v^2. For uniform grid spacing $\Delta x = \Delta y \equiv \Delta$ and equal partitioning of WaCM measurement errors between the u and v components so that $\sigma_u^2 = \sigma_v^2 \equiv \sigma_{u,v}^2 = \sigma_{spd}^2/2$, the sums on the right sides of (B4a) and (B5a) are exactly the same. The alongshore wavenumber spectra of the smoothed divergence and vorticity noise are then the same. The resulting analytical expression is shown by the green lines in the bottom nine panels of Fig. 4 for measurement noise with speed standard deviations of $\sigma_{spd} = 0.50$, 0.25 and 0.10 m s^{-1} and half-power filter cutoff wavelengths of $\lambda_c = 50$, 100 and 150 km.

References

Arbic, B. K., 2022: Incorporating tides and internal gravity waves within global ocean general circulation models: A review. *Prog. Oceanogr.*, **206**, doi.org/10.1016/j.pocean.2022.102824.

Ardhuin, F., and 29 others, 2018: Measuring currents, ice drift, and waves from space: the Sea Surface KInematics Multiscale monitoring (SKIM) concept. *Ocean Science*, **14**, 337–354 (http://dx.doi.org/10.5194/os-14-337-2018).

Chapron, B., F. Collard and F. Ardhuin, 2005: Direct measurements of ocean surface velocity from space: Interpretation and validation. *J. Geophys. Res.*, **110**, C07008, doi:101029/2004JC002809.

Chelton, D. B., and M. H. Freilich, 2005: Scatterometer-based assessment of 10-m wind analyses from the operational ECMWF and NCEP numerical weather prediction models. *Mon. Wea. Rev.*, **133**, 409–429.

Chelton, D. B., R. M. Samelson and J. T. Farrar, 2022: The effects of uncorrelated measurement noise on SWOT estimates of sea-surface height, velocity and vorticity. *J. Atmos. Oceanic Technol.*, **39**, 1053–1083.

Chelton, D. B., R. A. de Szoeke, M. G. Schlax, K. El Naggar and N. Siwertz, 1998: Geographical variability of the first-baroclinic Rossby radius of deformation. *J. Phys. Oceanogr.*, **28**, 433–460.

Chelton, D. B., M. G. Schlax, R. M. Samelson, J. T. Farrar, M. J. Molemaker, J. C. McWilliams and J. Gula, 2019: Prospects for future satellite estimation of small-scale variability of surface ocean velocity and vorticity. *Progr. Oceanogr.*, **173**, 256–350.

Da Silva, A. M., C. Young, and S. Levitus, 1994: *Algorithms and Procedures. Vol. 1, Atlas of Surface Marine Data 1994*,NOAA Atlas NESDIS 6, 74 pp.

Farrar, J. T., et al. (33 other authors), 2020: S-MODE: The Sub-Mesoscale Ocean Dynamics Experiment. In *IGARSS 2020 - 2020 IEEE International Geoscience and Remote Sensing Symposium*, pp. 3533–3536.

Molemaker, M. J., J. C. McWilliams and W. K. Dewar, 2015: Submesoscale instability and generation of mesoscale anticyclones near a separation of the California undercurrent. *J. Phys. Oceanogr.*, **45**, 613–629.

Risien, C. M., and D. B. Chelton, 2008: A global climatology of surface wind and wind stress fields from eight years of QuikSCAT scatterometer data. *J. Phys. Oceanogr.*, **38**, 2379–2413, doi:10.1175/2008JPO3881.1.

Rodríguez, E., 2018: On the optimal design of Doppler scatterometers. *Remote Sens.*, **10**, 1765, doi:10.3390/rs10111765.

Rodríguez, E., A. Wineteer, D. Perkovic-Martin, T. Gál, B. W. Stiles, N. Niamsuwan and R. Rodríguez Monje, 2018: Estimating ocean vector winds and currents using a Ka-band pencil-beam Doppler scatterometer. *Rem. Sens.*, **10**, 576.

Rodríguez E, M. Bourassa, D. B. Chelton, J. T. Farrar, D. Long, D. Perkovic-Martin and R. M. Samelson, 2019: The Winds and Currents Mission concept. *Front. Mar. Sci.*. **6**: 438, doi: 10.3389/fmars.2019.00438.

Villas Bôas, A. B., and 25 other authors, 2019: Integrated observations of global surface winds, currents, and waves: Requirements and challenges for the next decade. *Front. Mar. Sci.*, **6**: 425, doi: 10.3389/fmars.2019.00425.

Wentz, F. J., L. A. Mattox and S. Peteherych, 1986: New algorithms for microwave measurements of ocean winds with application o Seasat and SSM/I. *J. Geophys. Res.*, **91**, 2289–2307

Wineteer, A., H. S. Torres and E. Rodríguez, 2020: On the surface current measurement capabilities of spaceborne Doppler scatterometry. *Geophys. Res. Lett.*, **47**, 20GL090116. https://doi.org/10.1029/2020GL090116.